

A Compound Gaussian Network for Solving Linear Inverse Problems

Carter Lyons^{1,2}, Raghu G. Raj¹, and Margaret Cheney²

¹U.S. Naval Research Laboratory, Washington, D.C.

²Colorado State University, Fort Collins, CO

Abstract—For solving linear inverse problems, particularly of the type that appear in tomographic imaging and compressive sensing, this paper develops two new approaches. The first approach is an iterative algorithm that minimizes a regularized least squares objective function where the regularization is based on a compound Gaussian prior distribution. The compound Gaussian prior subsumes many of the commonly used priors in image reconstruction, including those of sparsity-based approaches. The developed iterative algorithm gives rise to the paper’s second new approach, which is a deep neural network that corresponds to an “unrolling” or “unfolding” of the iterative algorithm. Unrolled deep neural networks have interpretable layers and outperform standard deep learning methods. This paper includes a detailed computational theory that provides insight into the construction and performance of both algorithms. The conclusion is that both algorithms outperform other state-of-the-art approaches to tomographic image formation and compressive sensing, especially in the difficult regime of low training.

Index Terms—Machine learning, neural networks, inverse problems, nonlinear programming, least squares methods

NOTATION AND NOMENCLATURE

\mathbb{R}	Set of real numbers.
\mathbf{y}	$= [y_i] \in \mathbb{R}^n$. Boldface characters are vectors.
Y	$= [Y_{ij}] \in \mathbb{R}^{n \times m}$. Uppercase characters are matrices.
$(\cdot)^T$	Transpose of vector or matrix (\cdot) .
\odot	Hadamard product.
$D\{\mathbf{v}\}$	Diagonal matrix with v_1, v_2, \dots, v_n on the diagonal.
$A_{\mathbf{v}}$	$= AD\{\mathbf{v}\}$ for matrix A of compatible size.
$f(\mathbf{v})$	$= [f(v_i)]$ for componentwise function $f: \mathbb{R} \rightarrow \mathbb{R}$.
$\mathcal{P}_{a,b}(x)$	$= a + \text{ReLU}(x - a) - \text{ReLU}(x - b)$, for $a, b \in \mathbb{R}$, is a modified ReLU (mReLU) activation function.

I. INTRODUCTION

A. Image Reconstruction

MOTIVATED by the success of machine learning (ML) in image recognition and advances in deep learning, ML has been extended to various linear inverse problems—including the image reconstruction problems of tomographic

imaging and compressive sensing. Improving image reconstruction, the linear inverse problem of recovering an image from undersampled measurements, is an active area of research as it has widespread applicability including radar, sonar, medical, and tomographic imaging. Two prevalent classes of approaches are used in practice for image reconstruction, namely model-based and data-driven approaches.

First, model-based approaches incorporate certain assumptions, such as the expected prior density or sparsity level of the coefficients, into the image estimation method. Often, model-based methods apply an iterative algorithm designed to minimize an objective function. Examples include Iterative Shrinkage and Thresholding, Bayesian Compressive Sensing (BCS), Basis Pursuit, and Compressive Sampling Matching Pursuit (CoSaMP) [1]–[4]. Many previous works model the prior density, of the image coefficients, as a generalized Gaussian and solve a corresponding least squares problem with ℓ_p regularization [2, 4]–[6]. Alternatively, some previous works consider a compound Gaussian (CG) prior [7, 8], which is a class of densities subsuming generalized Gaussian and other densities as special cases, that better captures statistical properties of the coefficients of images [9]–[11].

Second, data-driven approaches learn the image reconstruction mapping directly by training a standard DNN on pairs of undersampled image measurements and image coefficients. Common DNNs in image reconstruction are structured upon a convolutional neural network (CNN), recurrent neural network, or a generative adversarial network [12]–[18].

Algorithm unrolling is a recent approach to image reconstruction, stemming from the original work of Gregor and LeCun [19], which combines the model-based and data-driven methods by structuring the layers of a DNN based on an iterative algorithm. Unlike a standard DNN, which acts as a black-box process, we have an understanding of the inner workings of an unrolled DNN from understanding the original iterative algorithm. Works utilizing algorithm unrolling have shown excellent performance in image reconstruction while offering simple interpretability of the network layers [20]. Examples of iterative imaging algorithms that have been unrolled include: iterative shrinkage and thresholding [19, 21]–[23], alternating direction method of multipliers [24], proximal gradient descent [25, 26], and half-quadratic splitting [27]. This work generalizes on initial work from [28] and provides further experimental and theoretical results.

Let $\mathbf{I} \in \mathbb{R}^n$ be a vectorized image or, in general, a signal

carter.lyons@colostate.edu
raghu.raj@nrl.navy.mil
margaret.cheney@colostate.edu

This work was sponsored by the Office of Naval Research via the NRL base program.

This material is based upon research supported in part by, the U. S. Office of Naval Research under award number N00014-21-1-2145 and by the Air Force Office of Scientific Research under award number FA9550-21-1-0169.

that has a representation $\mathbf{I} = \Phi \mathbf{c}$ with respect to (w.r.t) a dictionary, $\Phi \in \mathbb{R}^{n \times n}$, and coefficients, $\mathbf{c} \in \mathbb{R}^n$. An example, Φ is a wavelet transform and \mathbf{c} the wavelet coefficients. The linear measurement model is

$$\mathbf{y} = \Psi \Phi \mathbf{c} + \boldsymbol{\nu} \quad (1)$$

where $\mathbf{y} \in \mathbb{R}^m$ are the measurements produced by observing \mathbf{I} through a sensing matrix, $\Psi \in \mathbb{R}^{m \times n}$, with additive white noise, $\boldsymbol{\nu} \in \mathbb{R}^m$. In many applications of interest, $m \ll n$, which we refer to as the sparse sensing scenario. Image reconstruction, or estimation, is the linear inverse problem aimed at recovering the coefficients, \mathbf{c} , given the measurements, \mathbf{y} , sensing matrix, Ψ , and dictionary, Φ .

B. Contributions

In this work, we apply algorithm unrolling to a novel iterative image reconstruction algorithm that solves a regularized least squares (RLS) problem, which is fundamentally informed by the CG prior. Specifically, we:

- 1) Construct a novel iterative image estimation algorithm, named compound Gaussian least squares (CG-LS), to solve (1) with general Ψ and Φ matrices. A RLS optimization is the foundation for CG-LS where the regularization enforces a CG prior on the image coefficients. We provide experimental results illustrating the effectiveness of CG-LS in tomographic imaging.
- 2) Apply algorithm unrolling to CG-LS generating a DNN named CG-Net. Train and validate CG-Net on tomographic imaging and compressive sensing problems using wavelet and discrete cosine dictionaries. The effectiveness of CG-Net to reconstruct images after training is evaluated and shown to outperform other state-of-the-art imaging algorithms, especially in the low training and low noise regimes.
- 3) Provide fundamental characterization of the existence and location of minimizers of the CG-LS cost function.
- 4) Derive convergence analysis of CG-LS to stationary points of the cost function under a two-block coordinate descent with one block estimated via steepest descent.

C. Compound Gaussian Prior

A fruitful way to formulate inverse problems in imaging is by Bayesian estimation. In particular, consider the RLS estimate of \mathbf{c} from (1) $\hat{\mathbf{c}} = \arg \min \|\mathbf{y} - \Psi \Phi \mathbf{c}\|_2^2 + R(\mathbf{c})$, which can, equivalently, be viewed as a maximum a posteriori (MAP) estimation when the regularization satisfies $R(\mathbf{c}) \propto \log(p(\mathbf{c}))$. Therefore, the choice of regularization, $R(\mathbf{c})$, or prior density, $p(\mathbf{c})$, of the coefficients, \mathbf{c} , is a crucial component to incorporate domain level knowledge into the image reconstruction problem. Many previous works have employed a generalized Gaussian prior including a Gaussian prior, corresponding to a Tikhonov regression, [29, 30] or a Laplacian prior, as is predominant in the compressive sensing (CS) framework, [1, 2, 4]–[6, 31]. Additional regularizations, not derived from a specific prior density, have been implemented for image reconstruction including total variation norm [31]–[33] and deep learning-based regularization [17, 25, 26, 34].

Through the study of the statistics of image sparsity coefficients, it has been shown that coefficients of natural images exhibit self-similarity, heavy-tailed marginal distributions, and self-reinforcement among local coefficients [10]. Such properties are not encompassed by the generalized Gaussian prior typically assumed for the image coefficients. Instead, a class of densities known as CG densities [35], or Gaussian scale mixtures [9, 10], better capture statistical properties of natural images and images from other modalities such as radar [11, 36]. A useful formulation of the CG prior lies in modeling the coefficients of images as

$$\mathbf{c} = \mathbf{z} \odot \mathbf{u} \quad (2)$$

such that $\mathbf{z} = h(\mathbf{X})$, where $h : \mathbb{R} \rightarrow \mathbb{R}$ is a componentwise, positive, nonlinear function, \mathbf{X} follows a multi-scale Gaussian tree process [7, 10], $\mathbf{u} \sim \mathcal{N}(\mathbf{0}, \Sigma_u)$, and \mathbf{u} and \mathbf{z} are independent random variables. In Appendix VI-E, Proposition 7 shows the CG prior subsumes many well-known distributions including the generalized Gaussian. Additionally, Proposition 8 in Appendix VI-E provides the specific nonlinearity, h , producing a Laplace prior allowing an interpretation of the CG prior as a generalization of CS work.

Previously, the CG prior has been used, with $h(x) = \sqrt{\exp(x/\alpha)}$ for $\alpha \in (0, \infty)$, in a hierarchical Bayesian MAP estimate of wavelet and discrete cosine transformation (DCT) coefficients [7, 8]. This algorithm produces reconstructed images with superior quality, measured by the structural similarity index (SSIM), over other state-of-the-art CS techniques [7]. Furthermore, the CG prior, under a single random scale variable has been successfully used for image denoising [37] and hyperspectral image compressive sensing [38].

D. Deep Neural Networks and Algorithm Unrolling

A feedforward DNN can be viewed as a composition of multiple parameterized vector input and vector output functions. Each function is known as a layer and the function output dimension is known as the number of hidden units in the layer [39]. That is, let $\mathbf{L}_0, \mathbf{L}_1, \dots, \mathbf{L}_K$ denote the ordered $K + 1$ DNN layers, for fixed $K \geq 1$, where we assume each layer $\mathbf{L}_k \in \mathbb{R}^{d_k}$. For each $k \in \{1, 2, \dots, K\}$ a user-chosen function $\mathbf{f}_k : \mathbb{R}^{d_{i_1(k)}} \times \dots \times \mathbb{R}^{d_{i_j(k)}} \rightarrow \mathbb{R}^{d_k}$, that is parameterized by $\boldsymbol{\theta}_k$, defines \mathbf{L}_k as

$$\mathbf{L}_k \equiv \mathbf{f}_k(\mathbf{L}_{i_1(k)}, \dots, \mathbf{L}_{i_j(k)}; \boldsymbol{\theta}_k)$$

where $\mathcal{I}_k := \{i_1(k), \dots, i_j(k)\} \subseteq \{0, 1, \dots, k-1\}$ are the indices of layers used in computing \mathbf{L}_k . Fully connected networks, as an example, use $\mathcal{I}_k = \{k-1\}$ and

$$\mathbf{L}_k \equiv \mathbf{f}_k(\mathbf{L}_{k-1}; \boldsymbol{\theta}_k = [W_k, \mathbf{b}_k]) = \sigma(W_k \mathbf{L}_{k-1} + \mathbf{b}_k)$$

where $W_k \in \mathbb{R}^{d_k \times d_{k-1}}$, $\mathbf{b}_k \in \mathbb{R}^{d_k}$, and σ is a componentwise activation function. The initial layer \mathbf{L}_0 is known as the input layer and is assigned the measurement data that is provided to the DNN. Intermediate layers $\mathbf{L}_1, \dots, \mathbf{L}_{K-1}$ are known as hidden layers and the final layer \mathbf{L}_K is the output layer.

A DNN learns, or trains, its parameters, $\boldsymbol{\Theta} = (\boldsymbol{\theta}_1, \dots, \boldsymbol{\theta}_K)$, by optimizing a loss function $\mathcal{L}(\boldsymbol{\Theta})$ over a training dataset $\mathcal{D} = \{(\tilde{\mathbf{y}}_i, \tilde{\mathbf{c}}_i) : i = 1, 2, \dots, N_s\}$ where each $(\tilde{\mathbf{y}}_i, \tilde{\mathbf{c}}_i)$

satisfies equation (1). Let $\tilde{\mathbf{c}}(\tilde{\mathbf{y}}_i; \Theta)$ denote the DNN output given the input $\tilde{\mathbf{y}}_i$. Then the loss function is defined as $\mathcal{L}(\Theta) := \frac{1}{N_s} \sum_{i=1}^{N_s} L(\tilde{\mathbf{c}}(\tilde{\mathbf{y}}_i; \Theta), \tilde{\mathbf{c}}_i)$ where $L(\tilde{\mathbf{c}}(\tilde{\mathbf{y}}_i; \Theta), \tilde{\mathbf{c}}_i)$ is the loss, or error, between the network output, $\tilde{\mathbf{c}}(\tilde{\mathbf{y}}_i; \Theta)$, and the actual coefficients, $\tilde{\mathbf{c}}_i$. Common loss functions for image reconstruction neural networks include mean-squared error (MSE), normalized mean-squared error (NMSE), peak signal-to-noise ratio (PSNR), or SSIM [40]. After training the DNN, the cascade of function compositions can collectively model the desired transformation from an input space to an output space.

Algorithm unrolling creates a DNN by assigning the operations from each step k of the iterative algorithm as the function \mathbf{f}_k defining layer k . That is, layer k in the DNN should correspond to the output of k iterations of the original iterative algorithm. Then parameters, θ_k , on each step k of the iterative algorithm parameterize \mathbf{f}_k in the DNN [19, 20]. In training the unrolled DNN, each θ_k is learned, which optimizes the iterative algorithm to produce improved image estimates.

II. ITERATIVE ALGORITHM (CG-LS)

Let h be the componentwise, invertible, nonlinear function in the CG prior and $f = h^{-1}$. Defining $A = \Psi\Phi$, we consider the RLS cost function and estimate given respectively by

$$F(\mathbf{u}, \mathbf{z}) = \|\mathbf{y} - A(\mathbf{z} \odot \mathbf{u})\|_2^2 + \lambda \|\mathbf{u}\|_2^2 + \mu \|f(\mathbf{z})\|_2^2 \quad (3)$$

$$[\mathbf{u}^* \quad \mathbf{z}^*] = \arg \min_{\substack{\mathbf{u} \quad \mathbf{z}}} F(\mathbf{u}, \mathbf{z}). \quad (4)$$

Our CG-LS, given in Algorithm 1, is an iterative algorithm that, approximately, solves (4). The cost function (3) is a RLS where, as given by the CG prior, the coefficients are decomposed as $\mathbf{c} = \mathbf{z} \odot \mathbf{u}$ and the regularization is taken to be $R(\mathbf{c}) = R(\mathbf{u}, \mathbf{z}) = \lambda \|\mathbf{u}\|_2^2 + \mu \|f(\mathbf{z})\|_2^2$ to enforce normality of \mathbf{u} and $\mathbf{X} = f(\mathbf{z})$, a Gaussian tree process, as desired from the CG prior. We note that $R(\mathbf{c})$ is not exactly proportional to $\log(p(\mathbf{c}))$, as specified from the MAP estimate, as this is not analytically tractable for general h . Instead, $R(\mathbf{c})$ is an approximation capturing important statistical properties of the CG prior while also simplifying the optimization.

Due to the explicit joint estimation in (4), we optimize by block coordinate descent [41], which on iteration k produces

$$\mathbf{z}_k = \arg \min_{\mathbf{z} \in \mathcal{Z}^n} \|\mathbf{y} - A\mathbf{u}_{k-1}\mathbf{z}\|_2^2 + \mu \|f(\mathbf{z})\|_2^2 \quad (5)$$

$$\mathbf{u}_k = \arg \min_{\mathbf{u} \in \mathbb{R}^n} \|\mathbf{y} - A\mathbf{z}_k\mathbf{u}\|_2^2 + \lambda \|\mathbf{u}\|_2^2 \quad (6)$$

where $\mathcal{Z} \subseteq [0, \infty)$ is the domain of f . Convergence rates of block coordinate descent under different conditions for the cost function, such as convexity, have been proven [41]–[43]. As the optimization in (5) cannot be solved analytically, for most choices of f , we implement the steepest descent method to iteratively and approximately solve (5). Recall [44] that given a norm $\|\cdot\|$ on \mathbb{R}^n and differentiable function, $g(\mathbf{x}) : \mathbb{R}^n \rightarrow \mathbb{R}$, the steepest descent vector, $\mathbf{d} : \mathbb{R}^n \rightarrow \mathbb{R}^n$, is

$$\mathbf{d}(\mathbf{x}) = \|\nabla g(\mathbf{x})\|_* \left(\arg \min_{\|\mathbf{v}\|=1} \nabla g(\mathbf{x})^T \mathbf{v} \right) \quad (7)$$

where $\|\cdot\|_*$ is the dual norm given by $\|\mathbf{w}\|_* = \max_{\|\mathbf{v}\|=1} \mathbf{w}^T \mathbf{v}$. For instance the Euclidean norm produces $\mathbf{d}(\mathbf{x}) = -\nabla g(\mathbf{x})$.

Applying steepest descent to (5) we write \mathbf{z}_k^j as the estimate of \mathbf{z} on steepest descent step j of iteration k . For generality, we assume that a different norm may define each steepest descent step as is the case in Newton descent for a convex cost function with non-constant Hessian. Let $\mathbf{d}_k^j = \mathbf{d}_k^j(\mathbf{z})$ denote the descent vector corresponding to norm $\|\cdot\|_{*(k,j)}$, with dual norm $\|\cdot\|_{*(k,j)}$, for steepest descent step j of iteration k . Thus, \mathbf{z}_k^j is given by

$$\mathbf{z}_k^j = \mathbf{z}_k^{j-1} + \eta_k^{(j)} \mathbf{d}_k^j(\mathbf{z}_k^{j-1})$$

where $\eta_k^{(j)}$ is a step size determined by a backtracking line search [44]. Note, $\mathbf{d}_k^j = \mathbf{d}_k^j(\mathbf{z}) = \mathbf{d}_k^j(\mathbf{z}; \mathbf{u}_{k-1}, \mathbf{y})$ as \mathbf{d}_k^j is parameterized by \mathbf{u}_{k-1} and \mathbf{y} . Let J be the maximum number of steepest descent steps; then, for notation, we take $\mathbf{z}_k^J = \mathbf{z}_k = \mathbf{z}_k^0$.

Equation (6) has the well-known Tikhonov solution

$$\mathbf{u}_k = (A_{\mathbf{z}_k}^T A_{\mathbf{z}_k} + \lambda I)^{-1} A_{\mathbf{z}_k}^T \mathbf{y}. \quad (8)$$

Note, in practice, we will not calculate the inverse and instead solve a system of linear equations. Next, define the initial estimate of \mathbf{z} as $\mathbf{z}_0 = \mathcal{P}_{a,b}(A^T \mathbf{y})$ where the mReLU function $\mathcal{P}_{a,b}$ is applied elementwise to $A^T \mathbf{y}$. We remark that $\mathcal{P}_{a,b}$ is a projection operator onto the interval $[\min\{a, b\}, \max\{a, b\}]$. This eliminates negative values, as \mathbf{z} should have positive components, and limits the maximum values in the initial \mathbf{z} estimate. The initial \mathbf{u} estimate, denoted as \mathbf{u}_0 , is given by (8).

Finally, the gradient, $\nabla_{\mathbf{z}} F(\mathbf{u}, \mathbf{z})$, and a user-chosen parameter $\delta > 0$ determine convergence of CG-LS. On each steepest descent step j of iteration k , we check if $\|\nabla_{\mathbf{z}} F(\mathbf{u}_{k-1}, \mathbf{z}_k^{j-1})\|_{*(k,j)} < \delta$. When this holds, we exit the steepest descent steps taking $\mathbf{z}_k = \mathbf{z}_k^{j-1}$. Once $\|\nabla_{\mathbf{z}} F(\mathbf{u}_{k-1}, \mathbf{z}_k^0)\|_{*(k,1)} < \delta$ we say CG-LS has converged and return estimates \mathbf{u}_{k-1} and \mathbf{z}_{k-1} . Otherwise, CG-LS terminates after a user-chosen maximum number of iterations K .

Algorithm 1 Compound Gaussian Least Squares (CG-LS)

- 1: $\mathbf{z}_0 = \mathcal{P}_{a,b}(A^T \mathbf{y})$ and $\mathbf{u}_0 = (A_{\mathbf{z}_0}^T A_{\mathbf{z}_0} + \lambda I)^{-1} A_{\mathbf{z}_0}^T \mathbf{y}$
 - 2: **for** $k \in \{1, 2, \dots, K\}$ **do**
 - 3: \mathbf{z} ESTIMATION:
 - 4: $\mathbf{z}_k^0 = \mathbf{z}_{k-1}$
 - 5: **for** $j \in \{1, 2, \dots, J\}$ **do**
 - 6: **if** $\|\nabla_{\mathbf{z}} F(\mathbf{u}_{k-1}, \mathbf{z}_k^{j-1})\|_{*(k,j)} < \delta$ **then**
 - 7: **return** $\mathbf{z}_k = \mathbf{z}_k^{j-1}$
 - 8: **end if**
 - 9: Compute step size $\eta_k^{(j)}$ (backtracking line search)
 - 10: Compute descent vector $\mathbf{d}_k^j = \mathbf{d}_k^j(\mathbf{z}_k^{j-1}; \mathbf{u}_{k-1}, \mathbf{y})$
 - 11: $\mathbf{z}_k^j = \mathbf{z}_k^{j-1} + \eta_k^{(j)} \mathbf{d}_k^j(\mathbf{z}_k^{j-1}; \mathbf{u}_{k-1}, \mathbf{y})$
 - 12: **end for**
 - 13: $\mathbf{z}_k = \mathbf{z}_k^J$
 - 14: \mathbf{u} ESTIMATION:
 - 15: $\mathbf{u}_k = (A_{\mathbf{z}_k}^T A_{\mathbf{z}_k} + \lambda I)^{-1} A_{\mathbf{z}_k}^T \mathbf{y}$
 - 16: **end for**
- Output:** $\mathbf{c}^* = \mathbf{z}_K \odot \mathbf{u}_K$
-

A. Existence and Location of Minimizers

Here, we discuss the existence of minimizers to (3) along with details on their location that can be ensured through a sufficient scaling on the measurements, \mathbf{y} , or proper choices of CG-LS parameters, λ and μ . We remark that (3) is strongly convex in the \mathbf{u} block, with parameter at least 2λ , and thus has no local maxima.

Throughout the remainder of this paper we will assume that $f : \mathcal{Z} \rightarrow \mathbb{R}$ is a C^2 function defined on $\mathcal{Z} = (z_{\min}, \infty)$. While in theory f should be an invertible function we will not require this. Additionally, we assume that f is coercive on \mathcal{Z} , that is $\lim_{z \rightarrow z_{\min}} f(z) \rightarrow \pm\infty$ and $\lim_{z \rightarrow \infty} f(z) \rightarrow \pm\infty$. Now, we give a necessary and sufficient condition that any stationary point of (3) must satisfy.

Lemma 1. Define $\mathbf{v} : \mathcal{Z}^n \rightarrow \mathbb{R}^n$ and $\mathcal{F} : \mathcal{Z}^n \rightarrow \mathbb{R}^n$ by

$$\mathbf{v}(\mathbf{z}) = A^T(A_z A_z^T + \lambda I)^{-1} \mathbf{y} \quad (9)$$

$$\mathcal{F}(\mathbf{z}) = -2\lambda \mathbf{z} \odot \mathbf{v}(\mathbf{z}) \odot \mathbf{v}(\mathbf{z}) + 2\mu f'(\mathbf{z}) \odot f(\mathbf{z}). \quad (10)$$

Then (3) has a stationary point $[\mathbf{u}^*, \mathbf{z}^*]$ if and only if $\mathcal{F}(\mathbf{z}^*) = \mathbf{0}$ and $\mathbf{u}^* = \mathbf{z}^* \odot \mathbf{v}(\mathbf{z}^*)$.

Proof. Solving $\nabla_{\mathbf{u}} F(\mathbf{u}, \mathbf{z}) = \mathbf{0}$ and applying the Woodbury matrix identity gives $\mathbf{u} = \mathbf{z} \odot \mathbf{v}(\mathbf{z})$. Next, applying the Woodbury matrix identity to $\nabla_{\mathbf{z}} F(\mathbf{z} \odot \mathbf{v}(\mathbf{z}), \mathbf{z})$ produces (10). Therefore, $\nabla_{\mathbf{u}} F(\mathbf{u}, \mathbf{z}) = \nabla_{\mathbf{z}} F(\mathbf{u}, \mathbf{z}) = \mathbf{0}$ if and only if $\mathbf{z} = \mathbf{z}^*$ is a root of (10) and $\mathbf{u} = \mathbf{z}^* \odot \mathbf{v}(\mathbf{z}^*)$. \square

We remark that if $f(z)^2$ is strictly decreasing on an interval \mathcal{I} then, from Lemma 1, $\mathbf{z}^* \in \mathcal{Z}^n \setminus \mathcal{I}^n$ for any stationary point $[\mathbf{u}^*, \mathbf{z}^*]$ of (3). A particular application is when f is invertible and obtains a root, at z_0 , on \mathcal{Z} then $\mathbf{z}^* \in [z_0, \infty)^n$.

Next, we assume that the measurements, \mathbf{y} , have been scaled by a positive constant s . That is, $\mathbf{y} = s\tilde{\mathbf{y}}$ for $\tilde{\mathbf{y}}$ given by (1). Under certain conditions and choices of s , λ , and μ we gain significant insight into the location of a minimizer of (3).

Proposition 2. Let $f^2(z)$ be strictly convex and obtain an interior local minimum, at z_0 , on $[a, b] \subseteq \mathcal{Z}$. Then there exists positive s , λ , and μ such that (3) has a non-degenerate local minimizer $[\mathbf{u}^*, \mathbf{z}^*]$ where $\mathbf{z}^* \in [z_0, b]^n$ and $\mathbf{u}^* = \mathbf{z}^* \odot \mathbf{v}(\mathbf{z}^*)$.

A proof of Proposition 2 is given in Appendix VI-A. We remark that Proposition 2 extends optimization insights from the single variable function $f^2(z)$ to the multivariate cost function (3) that involves \mathbf{z} and \mathbf{u} . In particular, Proposition 2 is useful for choosing the correct scaling constant to match the mReLU interval, which is informed by intervals of convexity and roots of $f^2(z)$, defining the initial estimate of \mathbf{z} in Algorithm 1. Additionally, the convexity of $f^2(z)$ in conjunction with the scaling law revealed in Proposition 2 guarantees convexity of (5) and the existence of a unique stationary point within this convex region.

B. Convergence of CG-LS

For any norm, $\|\cdot\|$, on \mathbb{R}^n we remark that a Euclidean lower bound exists. That is, there exists a constant $0 < \gamma \leq 1$ such that $\|\cdot\| \geq \gamma \|\cdot\|_2$. Thus, for every CG-LS steepest descent

norm $\|\cdot\|_{(k,j)}$ with dual norm $\|\cdot\|_{*(k,j)}$ we let $\gamma_{(k,j)}$ and $\gamma_{*(k,j)}$ be the respective Euclidean bound constants.

To show Algorithm 1 converges, we first give a lower bound on the change in the cost function for a steepest descent step on \mathbf{z} . To simplify notation, define the function $G_k(\mathbf{z}) = F(\mathbf{u}_{k-1}, \mathbf{z})$.

Proposition 3. For every $k, j \in \mathbb{N}$, there exists a positive constant, $c_{(k,j)}$, such that Algorithm CG-LS satisfies

$$G_k(\mathbf{z}_k^{j-1}) - G_k(\mathbf{z}_k^j) \geq c_{(k,j)} \left\| \nabla G_k(\mathbf{z}_k^{j-1}) \right\|_{*(k,j)}^2. \quad (11)$$

A proof of Proposition 3 is given in Appendix VI-B. From Proposition 3, the sequence of cost function values, $\{G_k(\mathbf{z}_k^j)\}_{j=0}^\infty$, monotonically decreases, and when the gradient is large, we expect a large decrease in the cost function. Since $G_k(\mathbf{z}) \geq 0$, we know the sequence $\{G_k(\mathbf{z}_k^j)\}_{j=0}^\infty$ converges. That is, each steepest descent process in CG-LS will converge. To show convergence of CG-LS to a stationary point of (3), we apply Proposition 3 and similarly bound the change in the cost function over an iteration of CG-LS.

Theorem 4. Assume the Euclidean bound sequences $\{\gamma_{(k,1)}\}_{k=1}^\infty$ and $\{\gamma_{*(k,1)}\}_{k=1}^\infty$ are bounded below by $\gamma > 0$. Then CG-LS converges to a stationary point of (3). Furthermore, the sequence of minimum gradient dual norms satisfies

$$\min_{1 \leq k \leq K} \left\| \nabla F(\mathbf{u}_k, \mathbf{z}_k) \right\|_{*(k,1)}^2 \leq \mathcal{O}\left(\frac{1}{K}\right).$$

A proof of Theorem 4 is in Appendix VI-C and shows that CG-LS generates a monotonic decreasing sequence of cost function values. Combining Theorem 4 with the fact that (3) has no local maxima, Algorithm 1 is guaranteed to converge to a local minimum or saddle point of (3). As (3) is, in general, not convex, we cannot guarantee that Algorithm 1 converges to a local nor global minimum. Although, if Proposition 2 is also satisfied, we can guarantee convergence to a global minimizer of (3) relative to $[z_0, b]^n \times \mathbb{R}^n$.

We further strengthen our convergence results when Proposition 2 is satisfied. Let γ be given as in Theorem 4 and c from (27).

Theorem 5. Let Proposition 2 be satisfied with local minimizer $[\mathbf{u}^*, \mathbf{z}^*]$ corresponding to minimum value F^* . Then there exists a region $\mathcal{C} \subseteq \mathbb{R}^n \times \mathcal{Z}^n$ such that $[\mathbf{u}^*, \mathbf{z}^*] \in \mathcal{C}$ and (3) is strongly convex on \mathcal{C} with constant ℓ . Furthermore, for any $[\mathbf{u}_0, \mathbf{z}_0] \in \mathcal{C}$ we have for all $k \geq 0$

$$F(\mathbf{u}_k, \mathbf{z}_k) - F^* \leq (1 - 2\ell\gamma^2 c)^k (F(\mathbf{u}_0, \mathbf{z}_0) - F^*). \quad (12)$$

A proof of Theorem 5 is in Appendix VI-D. Theorem 5 shows a region around the local minimizer where (3) is strongly convex exists and thus we can guarantee a linear rate of convergence of the cost function values in this region.

C. Numerical Results

We test the CG-LS algorithm using gradient descent, which we denote by gCG-LS, and Newton descent, which we denote

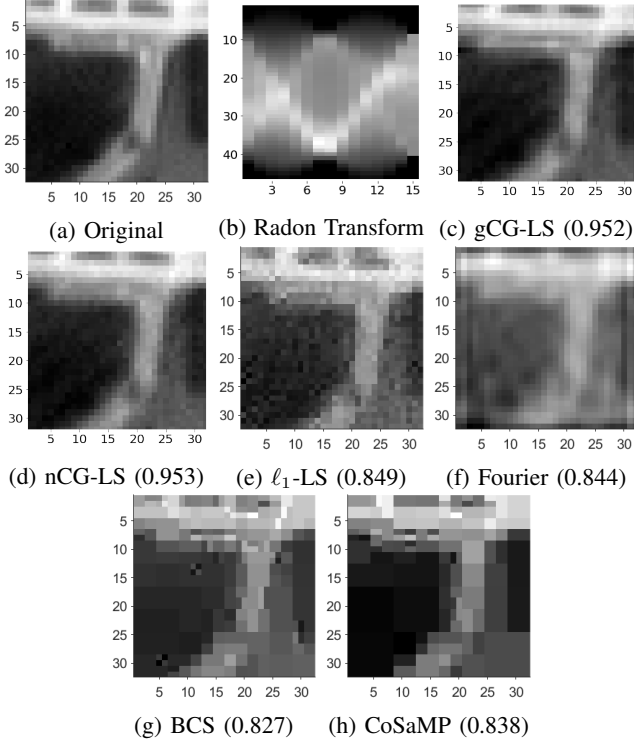


Fig. 1: Image reconstructions (SSIM) using our gCG-LS, our nCG-LS, ℓ_1 -LS, Fourier backprojection, Bayesian Compressive Sensing, and CoSaMP. The input to each algorithm is a vectorized (1b), which is the Radon transform of the original 32×32 image, (1a), at 15 uniformly spaced angles with a noise level of 60dB SNR. We observe that CG-LS outperforms all methods with nCG-LS slightly outperforming gCG-LS.

by nCG-LS, as the steepest descent method for updating \mathbf{z} . Note, the gradient and Hessian of (3) w.r.t \mathbf{z} are, respectively:

$$\nabla_{\mathbf{z}} F(\mathbf{u}, \mathbf{z}) = -2A_{\mathbf{u}}^T(\mathbf{y} - A_{\mathbf{u}}\mathbf{z}) + 2\mu f'(\mathbf{z}) \odot f(\mathbf{z}) \quad (13)$$

$$H_{F;\mathbf{z}}(\mathbf{u}, \mathbf{z}) = 2A_{\mathbf{u}}^T A_{\mathbf{u}} + 2\mu D\{h_f(\mathbf{z})\} \quad (14)$$

where

$$h_f(\mathbf{z}) = f''(\mathbf{z}) \odot f(\mathbf{z}) + f'(\mathbf{z}) \odot f'(\mathbf{z}). \quad (15)$$

We use 32×32 images from the CIFAR10 image dataset [45] and 64×64 images from the CalTech101 [46] image dataset. Each image has been converted to a single-channel grayscale image, scaled down by the maximum pixel value, and vectorized. A Radon transform, at a specified number of uniformly spaced angles, is performed on each image to which white noise is added producing noisy measurements, \mathbf{y} , at a specified signal-to-noise ratio (SNR). Finally, a biorthogonal wavelet transformation is applied to each image to produce the coefficients, \mathbf{c} .

For all simulations, we use $f(z) = \ln(z)$, $\mu = 2$, $K = 1000$, $J = 1$, and $\delta = 10^{-6}$. For measurements at an SNR of 60dB and 40dB, we take $\lambda = 0.3$ and $\lambda = 2$, respectively. Using nCG-LS requires (14) to be positive definite in the \mathbf{z} variable, which for $f(z) = \ln(z)$, is guaranteed when $\mathbf{z} \in (0, e)^n$. Informed by Proposition 2, we can guarantee a local minimizer lies in $[1, e)^n$ under sufficient scaling of the

input data. Therefore, in each nCG-LS test using 32×32 or 64×64 image measurements, we scale the input measurement by a factor, chosen empirically, of e^{-4} or e^{-6} , respectively. Additionally, we use an eigendecomposition on (14) to find the closest positive semi-definite matrix that is then used in the Newton descent step. Alternatively, we remark that the mReLU function $\mathcal{P}_{1,e}$ may be applied at each \mathbf{z} update in line 11 of Algorithm 1 to ensure (14) is positive semi-definite. Finally, we choose $\mathcal{P}_{a,b} = \mathcal{P}_{1,e}$ for nCG-LS whereas for gCG-LS we use $\mathcal{P}_{a,b} = \mathcal{P}_{1,e^2}$.

Fig. 1 contains the reconstruction of a 32×32 Barbara snippet for six iterative algorithms: gCG-LS, nCG-LS, ℓ_1 -least squares (ℓ_1 -LS) [6], Fourier backprojection (FBP) [47], BCS [3], and CoSaMP [4]. Each algorithm takes as input (1b) vectorized, which is a 60dB SNR Radon transform at 15 uniformly spaced angles. In (1b) the angle and distance are given on the x and y axes, respectively. Similarly, Fig. 2 contains the reconstruction of a 64×64 Barbara snippet from a 60dB SNR Radon transform at 15 uniformly spaced angles. We see by visual inspection and SSIM that both gCG-LS and nCG-LS produce superior reconstructions to the other iterative algorithms with nCG-LS slightly outperforming gCG-LS.

The superiority of CG-LS is further highlighted in Table I, which shows the average image reconstruction SSIM and PSNR along with 99% confidence intervals. Note, larger

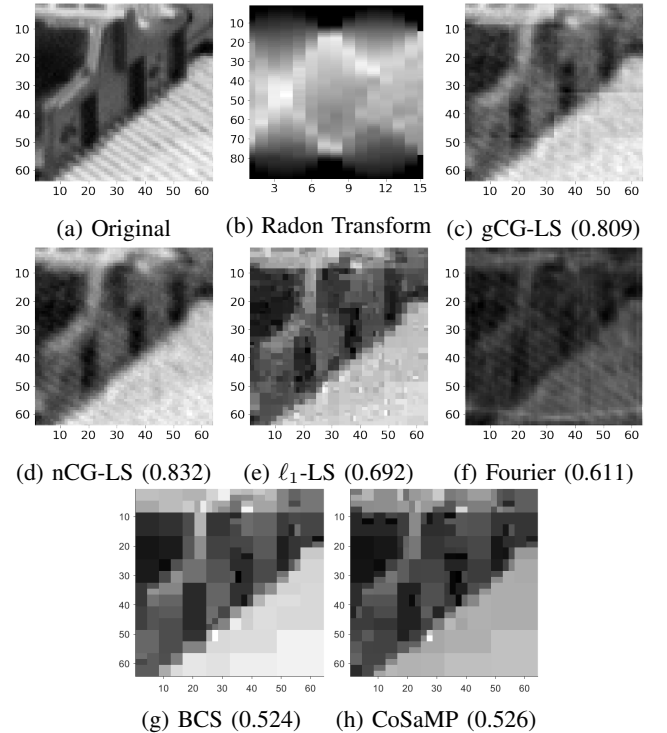


Fig. 2: Image reconstructions (SSIM) using our gCG-LS, our nCG-LS, ℓ_1 -LS, Fourier backprojection, Bayesian Compressive Sensing, and CoSaMP. The input to each algorithm is a vectorized (2b), which is the Radon transform of the original 64×64 image, (2a), at 15 uniformly spaced angles with a noise level of 60dB SNR. We observe that CG-LS outperforms all methods with nCG-LS slightly outperforming gCG-LS.

TABLE I: Average SSIM/PSNR with 99% confidence intervals for six image estimation algorithms including our gCG-LS and our nCG-LS. Each algorithm estimated two hundred, 32×32 and 64×64 images from Radon transform measurements taken at 15, 10, or 6 uniformly spaced angles. The measurement noise is set at 60dB or 40dB SNR. We find that CG-LS performs best in all noise and sparse sensing scenarios with nCG-LS, in **bold**, slightly outperforming gCG-LS, in *italics*.

		SSIM ($\times 10^2$)/PSNR for 32×32 images					
Angles	15	10		6			
SNR	60 dB	40 dB	60 dB	40 dB	60 dB	40 dB	
nCG-LS	91.3 \pm .59/28.0 \pm .39	87.0 \pm .97/26.2 \pm .28	83.6 \pm .82/24.8 \pm .39	80.6 \pm .94/24.0 \pm .32	70.0 \pm 1.1/21.7 \pm .37	68.0 \pm 1.2/21.3 \pm .35	
gCG-LS	<i>90.1 \pm .57/27.1 \pm .38</i>	<i>85.9 \pm .93/25.5 \pm .28</i>	<i>82.3 \pm .78/24.3 \pm .40</i>	<i>80.1 \pm .86/23.8 \pm .34</i>	<i>68.9 \pm 1.1/21.4 \pm .42</i>	<i>67.9 \pm 1.1/21.3 \pm .40</i>	
ℓ_1 -LS	86.6 \pm .58/26.0 \pm .42	72.7 \pm 1.6/22.1 \pm .35	74.5 \pm .93/22.8 \pm .42	67.2 \pm 1.1/21.2 \pm .29	55.2 \pm 1.3/19.4 \pm .42	52.5 \pm 1.2/18.9 \pm .36	
FBP	85.7 \pm .77/20.6 \pm .36	81.2 \pm 1.2/20.2 \pm .35	72.4 \pm 1.1/14.5 \pm .42	68.4 \pm 1.3/14.3 \pm .43	53.4 \pm 1.1/18.8 \pm .46	50.2 \pm 1.2/18.7 \pm .45	
BCS	77.4 \pm .96/22.7 \pm .43	74.1 \pm .93/22.1 \pm .34	62.4 \pm 1.2/19.9 \pm .44	60.4 \pm 1.2/19.6 \pm .42	44.6 \pm 1.5/17.3 \pm .45	44.1 \pm 1.5/17.2 \pm .44	
CoSaMP	75.9 \pm 1.0/22.4 \pm .48	71.2 \pm .98/21.3 \pm .34	61.7 \pm 1.2/19.5 \pm .44	58.6 \pm 1.1/18.9 \pm .36	35.5 \pm 1.5/14.8 \pm .48	32.4 \pm 1.3/14.2 \pm .43	

		SSIM ($\times 10^2$)/PSNR for 64×64 images					
Angles	15	10		6			
SNR	60 dB	40 dB	60 dB	40 dB	60 dB	40 dB	
nCG-LS	67.5 \pm 1.2/22.7 \pm .45	63.2 \pm 1.4/22.0 \pm .41	58.3 \pm 1.3/21.0 \pm .43	56.0 \pm 1.3/20.7 \pm .41	46.8 \pm 1.3/19.0 \pm .42	45.7 \pm 1.3/18.9 \pm .42	
gCG-LS	<i>65.5 \pm 1.1/22.0 \pm .43</i>	<i>61.3 \pm 1.3/21.4 \pm .39</i>	<i>56.9 \pm 1.2/20.5 \pm .44</i>	<i>54.4 \pm 1.2/20.3 \pm .42</i>	<i>45.4 \pm 1.4/18.5 \pm .47</i>	<i>44.0 \pm 1.2/18.4 \pm .46</i>	
ℓ_1 -LS	61.6 \pm 1.3/21.5 \pm .49	45.3 \pm 1.7/18.3 \pm .46	48.7 \pm 1.4/19.4 \pm .46	40.7 \pm 1.1/18.0 \pm .40	33.7 \pm 1.4/16.7 \pm .44	30.0 \pm 1.0/16.2 \pm .43	
FBP	54.6 \pm 1.3/15.3 \pm .57	48.1 \pm 1.4/14.9 \pm .56	41.5 \pm 1.1/9.33 \pm .66	36.2 \pm 1.1/9.13 \pm .65	27.6 \pm .81/14.4 \pm .71	23.6 \pm .76/14.1 \pm .70	
BCS	54.3 \pm 1.9/19.4 \pm .49	52.3 \pm 1.8/19.1 \pm .47	40.7 \pm 1.9/17.2 \pm .47	39.6 \pm 1.9/17.0 \pm .46	29.1 \pm 1.9/15.2 \pm .49	28.9 \pm 1.9/15.2 \pm .48	
CoSaMP	54.2 \pm 2.0/19.2 \pm .49	51.5 \pm 1.7/18.6 \pm .45	41.1 \pm 2.1/16.8 \pm .48	40.0 \pm 1.9/16.6 \pm .46	24.8 \pm 1.6/13.5 \pm .47	24.3 \pm 1.5/13.4 \pm .46	

SSIM and PSNR values correspond to image reconstructions that are visually closer to the original image. One reason our method outperforms the comparative methods may be attributed to the relatively low sparsity level of the wavelet coefficients, \mathbf{c} , which CG-LS can manage while ℓ_1 -LS, BCS, and CoSaMP require a sufficiently high signal sparsity for superb performance. Although, CG-LS is slower, as shown in Table V.

III. CG-NET

A. Network Structure

We create a DNN by applying algorithm unrolling to CG-LS in Algorithm 1. CG-Net has a structure shown in Fig. 3 and consists of an input layer, L_0 , an initialization layer, Z_0 , an initial \mathbf{u} layer U_0 , K blocks given in Fig. 3b, and an output layer, O . Two main functions, $\mathbf{f}_k : \mathbb{R}^n \times \mathbb{R}^m \rightarrow \mathbb{R}^n$ and $\mathbf{g}_k^j : \mathbb{R}^n \times \mathbb{R}^n \times \mathbb{R}^m \rightarrow \mathbb{R}^n$, define the CG-Net layers. Each $\mathbf{f}_k(\mathbf{z}, \mathbf{y}) \equiv \mathbf{f}_k(\mathbf{z}, \mathbf{y}; \lambda_k)$, which is parameterized by a scalar λ_k , corresponds to updating \mathbf{u} as

$$\mathbf{f}_k(\mathbf{z}, \mathbf{y}) := (A_{\mathbf{z}}^T A_{\mathbf{z}} + \lambda_k I)^{-1} A_{\mathbf{z}}^T \mathbf{y}.$$

Next, each $\mathbf{g}_k^j(\mathbf{z}, \mathbf{u}, \mathbf{y}) \equiv \mathbf{g}_k^j(\mathbf{z}, \mathbf{u}, \mathbf{y}; a_k^j, b_k^j, \eta_k^{(j)}, \mathbf{d}_k^j)$, which is parameterized by a descent vector, \mathbf{d}_k^j , step size, $\eta_k^{(j)}$ and mReLU parameters a_k^j and b_k^j , corresponds to updating \mathbf{z} as

$$\mathbf{g}_k^j(\mathbf{z}, \mathbf{u}, \mathbf{y}) := \mathcal{P}_{a_k^j, b_k^j} \left(\mathbf{z} + \eta_k^{(j)} \mathbf{d}_k^j(\mathbf{z}; \mathbf{u}, \mathbf{y}) \right). \quad (16)$$

In CG-LS, the step size, $\eta_k^{(j)}$, is found by a backtracking line search, which we cannot implement in CG-Net. Thus, the application of the mReLU activation function, $\mathcal{P}_{a,b}$, at each steepest descent step serves to guarantee the next step is not too large and stays within \mathcal{Z} .

Now, we mathematically detail the CG-Net layers:

$L_0 = \mathbf{y}$ is the input measurements to the network

$Z_0 = \mathcal{P}_{a_0, b_0}(A^T \mathbf{y})$ is the initial estimate of \mathbf{z} from line 1 of Algorithm 1.

$U_0 = \mathbf{f}_0(Z_0, \mathbf{y})$ is the initial estimate of \mathbf{u} corresponding to line 1 of Algorithm 1.

The k th CG-Net block, shown in Fig. 3b, consists of layers:

$Z_k^j = \mathbf{g}_k^j(Z_k^{j-1}, U_{k-1}, \mathbf{y})$ is \mathbf{z} on steepest descent step j of iteration k , corresponding to line 11 in Algorithm 1.

$U_k = \mathbf{f}_k(Z_k^j, \mathbf{y})$ is \mathbf{u} on iteration k , corresponding to line 15 in Algorithm 1.

$O = U_K \odot Z_K^J$ is the estimated wavelet coefficients produced by CG-Net.

Note, to simplify notation, we let $Z_k^0 = Z_{k-1}^J$. CG-Net contains $K + 1$ estimation layers for \mathbf{u} , KJ steepest descent step layers for \mathbf{z} , one input, one output, and one initialization layer. Thus, CG-Net contains $K(J + 1) + 4$ layers in total.

B. Network Parameters and Loss Functions

We further detail the parameters that will be learned by CG-Net. For every $k = 0, 1, \dots, K$ the layer U_k is parameterized by regularization scalar, $\lambda_k > 0$. In Algorithm 1, every λ_k is taken to be the same constant, λ from (3), but we increase the trainability of CG-Net by allowing different λ_k at each layer updating \mathbf{u} . The initialization layer, Z_0 , is parameterized by two positive real numbers $a_0 > z_{\min}$ and $b_0 > z_{\min}$, which are applied through the mReLU function, \mathcal{P}_{a_0, b_0} .

Next, for each Z_k^j layer, defined by (16), we implement the steepest descent vector $\mathbf{d}_k^j(\mathbf{z}; \mathbf{u}) = -B_k^j \nabla_{\mathbf{z}} F(\mathbf{z}; \mathbf{u})$ for a positive definite matrix B_k^j that will be learned in CG-Net. Note, this descent vector is the steepest descent based upon the quadratic norm $\|\cdot\|_{(B_k^j)^{-1}}$. Thus, CG-Net can be understood as learning the quadratic norm defining every steepest descent step that optimally traverses the landscape of the cost function in (5). For matrix L , let Q and Λ be the eigendecomposition of $(L + L^T)/2$. That is, $(L + L^T)/2 = Q\Lambda Q^T$. Define, for small $\epsilon > 0$, the diagonal matrix Λ_ϵ as $[\Lambda_\epsilon]_{ii} = \max\{\Lambda_{ii}, \epsilon\}$ and let

$$P_\epsilon(L) = Q\Lambda_\epsilon Q^T. \quad (17)$$

That is, $P_\epsilon(L)$ can be viewed as the closest symmetric, real-valued matrix with minimum eigenvalue of ϵ to $(L + L^T)/2$ as measured by the Frobenius norm. We enforce B_k^j to be positive definite by learning a lower triangular matrix L_k^j and setting

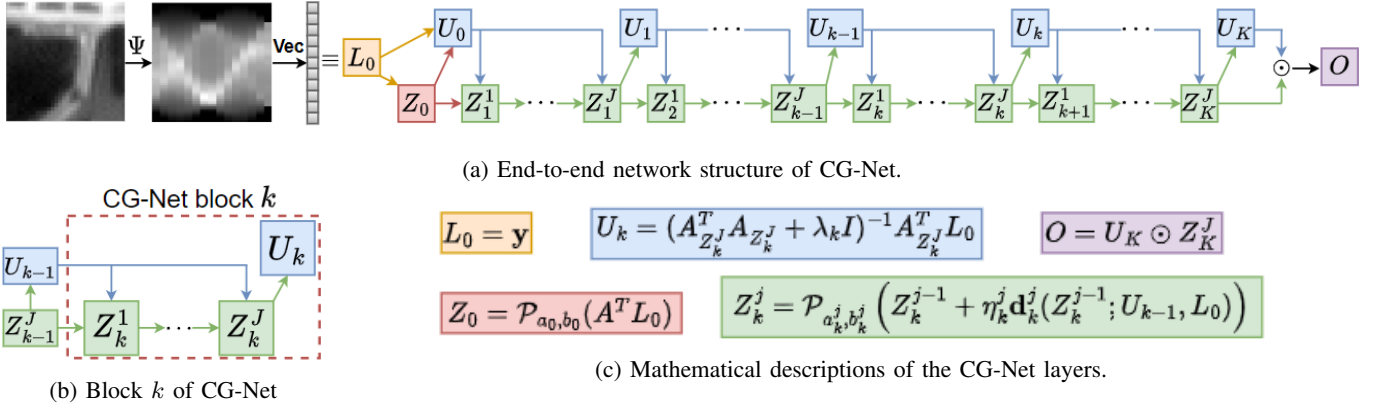


Fig. 3: End-to-end network structure for CG-Net, the unrolled deep neural network of Algorithm 1, is shown in (3a). A mathematical description of each layer is given in (3c). CG-Net consists of an input layer, L_0 , initialization layer, Z_0 , output layer, O , and K CG-Net blocks (3b). Each CG-Net block, k , contains J steepest descent layers, Z_k^1, \dots, Z_k^J , and a single Tikhonov layer, U_k . Every layer takes the measurements, $L_0 \equiv \mathbf{y}$, as an input so these connections are omitted for clarity.

$B_k^j = P_\epsilon(L_k^j)$. Therefore, CG-Net layer Z_k^j is parameterized by a lower triangular matrix L_k^j defining the steepest descent vector

$$\mathbf{d}_k^j(\mathbf{z}; \mathbf{u}) = -P_\epsilon(L_k^j) \nabla_{\mathbf{z}} F(\mathbf{u}, \mathbf{z}).$$

Additionally, as $\nabla_{\mathbf{z}} F(\mathbf{u}, \mathbf{z})$, given in (13), depends on the regularization scalar μ , layer Z_k^j is parameterized by regularization scalar μ_k^j . Furthermore, layer Z_k^j is parameterized by the step size $\eta_k^{(j)}$, which we take to be a diagonal matrix. That is, instead of learning a single constant to scale the steepest descent vector \mathbf{d}_k^j we learn a different constant to scale each component of \mathbf{d}_k^j separately. Finally, layer Z_k^j learns positive real numbers $a_k^j > z_{\min}$ and $b_k^j > z_{\min}$, which are applied through the mReLU activation function, $\mathcal{P}_{a_k^j, b_k^j}$, in (16).

Fix a small real-valued $\epsilon > 0$. We remark that to ensure $\lambda_k > 0$ and $a_0, b_0, a_k^j, b_k^j > z_{\min}$ in implementation we use $\max\{\lambda_k, \epsilon\}$ in place of λ_k , $\max\{a_0, z_{\min} + \epsilon\}$ in place of a_0 , and similarly for b_0, a_k^j , and b_k^j .

In total, CG-Net has $K \left(\frac{J}{2} (n(n+3) + 6) \right) + 3$ parameters

$$\Theta = \left\{ \lambda_0, a_0, b_0, \lambda_k, \mu_k^j, L_k^j, \eta_k^{(j)}, a_k^j, b_k^j \right\}_{k=1,2,\dots,K}^{j=1,2,\dots,J}$$

where n is the image size. The CG-Net parameters are trained by minimizing a loss function involving the SSIM image quality metric [40], namely for $\mathcal{B} \subset \mathcal{D}$ a batch of data points

$$\mathcal{L}_{\mathcal{B}}(\Theta) = \frac{1}{|\mathcal{B}|} \sum_{(\tilde{\mathbf{y}}_i, \tilde{\mathbf{c}}_i) \in \mathcal{B}} (1 - \text{SSIM}(\Phi \tilde{\mathbf{c}}(\tilde{\mathbf{y}}_i; \Theta), \Phi \tilde{\mathbf{c}}_i))$$

This cost function is optimized through adaptive moment estimation (Adam) [48], which is a stochastic gradient-based optimizer. Other common optimization methods include stochastic gradient descent, RMSprop, and Adadelta [48]. The gradient $\nabla_{\Theta} \mathcal{L}_{\mathcal{B}}$ for Adam is calculated via backpropagation through the network, which we implement with automatic differentiation [49] using Tensorflow.

C. Numerical Results

Given a sensing matrix, Ψ , dictionary, Φ , and noise level in SNR, we create a set of training and testing measurement-

coefficient pairs, (\mathbf{y}, \mathbf{c}) , as in Section II-C, that we use to train and evaluate a CG-Net. For network size, CG-Net running on 32×32 or 64×64 image measurements use $(K, J) = (20, 1)$ or $(K, J) = (5, 1)$, respectively. The network sizes were chosen empirically such that the time to complete one image reconstruction was reasonably quick while still producing excellent reconstructions on a validation set of test images. We let $f(z) = \ln(z)$ and initialize $a_0 = 1, b_0 = \exp(2)$, every $\eta_k^{(j)} = \frac{1}{2}I$, all $\mu_k^j = 2$, each $a_k^j = \frac{8}{10}$, all $b_k^j = \exp(3)$, and every $L_k^j = I$. Note, for CG-Net running on 32×32 images we only learn the diagonal and sub-diagonal in L_k^j constraining B_k^j to be a tridiagonal matrix. Finally, we initialize $\lambda_k = 0.3$ for 60dB SNR noise level and $\lambda_k = 2$ all other noise levels. Each CG-Net was trained for 20 epochs, using a learning rate of 10^{-3} , with early stopping implemented when the model overfits a validation dataset.

Shown in Fig. 4 is the average SSIM quality, over 200 test image reconstructions, for CG-Net, memory augmented deep unfolding network (MADUN) [21], and ISTA-Net⁺ [22] when each is trained on a varying amount of training data. MADUN and ISTA-Net⁺ are two DNNs formed by algorithm unrolling. Also compared was ReconNet [12], a standard CNN for image reconstructions, which was significantly the lowest performing and thus was omitted from Fig. 4. We consider small sets of training data specifically of size 1000, 500, 100, and 20 measurement, coefficient pairs. In Fig. 4a, 4b, and 4c we see when reconstructing images from Radon transforms with a noise level of 60dB SNR that CG-Net outperforms all comparative methods and does so significantly in low training. Similarly, in the low training and sparse sensing regimes of Fig. 4d, 4e, and 4f, where the SNR has decreased, we still observe that CG-Net outperforms all comparative methods. We believe this is due to the initialization of CG-Net corresponding precisely to CG-LS and thereby incorporating the powerful statistical CG prior. Also, unlike other algorithm unrolling methods, we do not replace any part of the optimization with a CNN, or another neural network, that is learned completely from scratch and likely overfits quickly in low training. Although,

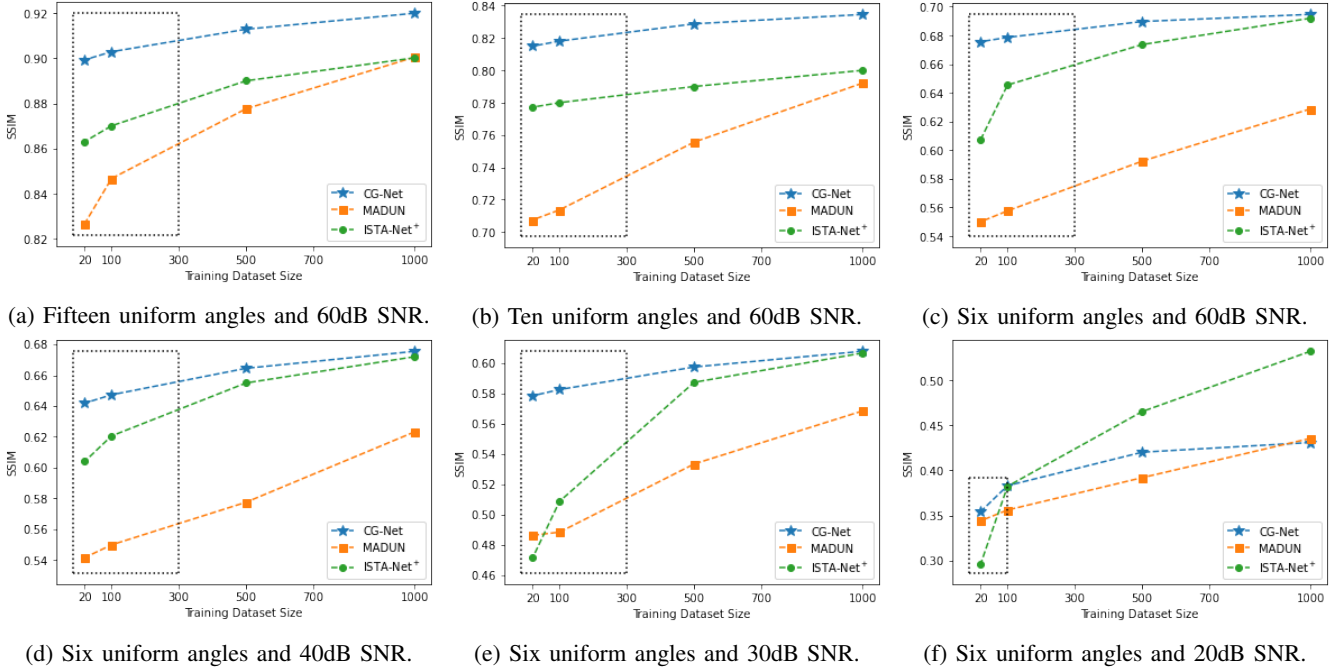


Fig. 4: Average test image reconstruction SSIM when varying the amount of data in training three machine learning-based image reconstruction methods. Here, the sensing matrices, Ψ , are a Radon transform at 15, 10, or 6 uniformly spaced angles and the sparsity dictionary, Φ , is a biorthogonal wavelet transform. The measurement noise level is set at either 60dB, 40dB, 30dB, or 20dB SNR. Our method, CG-Net, significantly outperforms all comparative methods, as highlighted in the boxed region, in the low training and low noise regimes. The 20 training samples scenario is further detailed in Table II.

TABLE II: Average SSIM/PSNR with 99% confidence intervals for four machine learning-based image reconstruction methods. Each method reconstructed two hundred, 32×32 and two hundred, 64×64 images, after training on a set of 20 samples. Here, the sensing matrices, Ψ , are a Radon transform at 15, 10, or 6 uniformly spaced angles and the dictionary, Φ , is a biorthogonal wavelet transform. The measurement noise level is set at 60dB or 40dB SNR. In all cases, our method CG-Net, highlighted in **bold**, outperforms the other approaches. Samples from these tests are visualized in Fig. 5, Fig. 6, and Fig. 7.

SSIM($\times 10^2$)/PSNR for 32×32 images								
Angles SNR	15		10		6			
	60 dB	40 dB	60 dB	40 dB	60 dB	40 dB		
CG-Net	89.9 \pm .56/27.7 \pm .38	84.4 \pm .87/25.5 \pm .28	81.5 \pm .83/24.8 \pm .40	77.4 \pm .83/23.8 \pm .34	67.6 \pm 1.2/21.8 \pm .40	64.2 \pm 1.2/21.3 \pm .40		
MADUN	82.6 \pm .82/24.7 \pm .29	80.4 \pm .92/24.1 \pm .28	70.7 \pm 1.0/22.1 \pm .28	68.4 \pm 1.1/21.7 \pm .27	54.9 \pm 1.2/19.5 \pm .31	54.2 \pm 1.1/19.3 \pm .32		
ISTA-Net ⁺	86.3 \pm .59/24.3 \pm .39	80.5 \pm .95/21.0 \pm .31	77.7 \pm .92/22.7 \pm .35	71.0 \pm 1.0/20.7 \pm .31	60.7 \pm 1.3/19.4 \pm .35	60.4 \pm 1.4/18.9 \pm .34		
ReconNet	19.6 \pm 1.4/15.8 \pm .32	19.0 \pm 1.5/15.2 \pm .31	18.7 \pm 1.6/14.9 \pm .32	18.3 \pm 1.6/15.0 \pm .32	17.7 \pm 1.5/14.6 \pm .32	17.1 \pm 1.6/14.5 \pm .31		

SSIM($\times 10^2$)/PSNR for 64×64 images								
Angles SNR	15		10		6			
	60 dB	40 dB	60 dB	40 dB	60 dB	40 dB		
CG-Net	65.4 \pm 1.2/22.8 \pm .46	60.6 \pm 1.3/22.0 \pm .41	56.6 \pm 1.3/21.1 \pm .44	53.1 \pm 1.2/20.7 \pm .41	45.7 \pm 1.3/19.1 \pm .43	43.1 \pm 1.2/18.9 \pm .41		
MADUN	52.7 \pm 1.2/19.8 \pm .43	47.0 \pm 1.3/18.5 \pm .49	45.5 \pm 1.4/19.0 \pm .42	43.6 \pm 1.0/19.1 \pm .39	35.2 \pm .98/17.8 \pm .37	34.1 \pm 1.1/17.6 \pm .41		
ISTA-Net ⁺	50.9 \pm 1.2/18.1 \pm .39	52.8 \pm 1.5/19.1 \pm .39	46.9 \pm 1.3/17.8 \pm .36	25.0 \pm 1.2/14.7 \pm .36	38.5 \pm 1.5/18.9 \pm .37	35.7 \pm 1.4/18.5 \pm .37		
ReconNet	12.9 \pm .97/14.0 \pm .38	11.3 \pm .92/13.5 \pm .36	11.5 \pm .94/13.7 \pm .37	11.0 \pm .91/13.6 \pm .38	10.6 \pm .96/13.4 \pm .38	9.40 \pm .90/13.1 \pm .38		

we remark that with greater noise and higher training CG-Net can sometimes perform lower than comparative methods.

The lowest training dataset size of 20 is further detailed in Table II, which displays the average SSIM and PSNR plus 99% confidence intervals over 200 test image reconstructions for CG-Net, MADUN, ISTA-Net⁺, and ReconNet. We see that CG-Net significantly outperforms all comparative methods. For a visual comparison of the four methods, Fig. 5 shows reconstructions, plus SSIM values, of a Barbara snippet from a Radon transform at 15 uniformly spaced angles with a noise level of 60dB SNR. Next, Fig. 6 shows the reconstructions of a dog image from a Radon transform at 10 uniformly spaced

angles with a noise level of 60dB SNR. Additionally, Fig. 7 shows the reconstructions of a truck image from a Radon transform at 6 uniformly spaced angles with a noise level of 60dB SNR. All reconstructions are performed after training on a dataset of 20 samples. In all figures, we see CG-Net producing higher quality images visually and by SSIM than the three comparison methods.

To further highlight the applicability of CG-Net we consider alternative sensing matrices, Ψ , and dictionaries, Φ as summarized in Table III. As typical in CS applications, we consider $\Psi \in \mathbb{R}^{m \times n}$ as a Gaussian matrix where $\frac{m}{n}$ is the sampling ratio. We consider a DCT as an alternative dictionary. In these

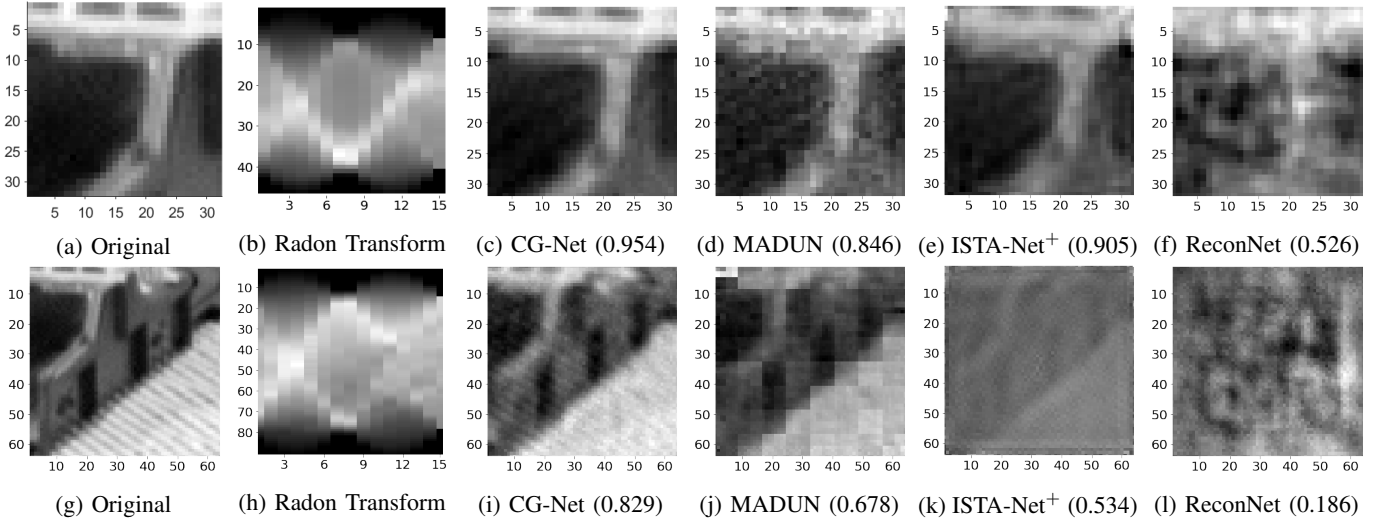


Fig. 5: Image reconstructions (SSIM) using CG-Net, MADUN, ISTA-Net⁺, and ReconNet for 32×32 and 64×64 Barbara images. The sensing matrix, Ψ , is a Radon transform at 15 uniformly spaced angles, the dictionary, Φ , is a biorthogonal wavelet transformation, and the noise level is 60dB SNR. Our method CG-Net, shown in (5c) and (5i), performs best.

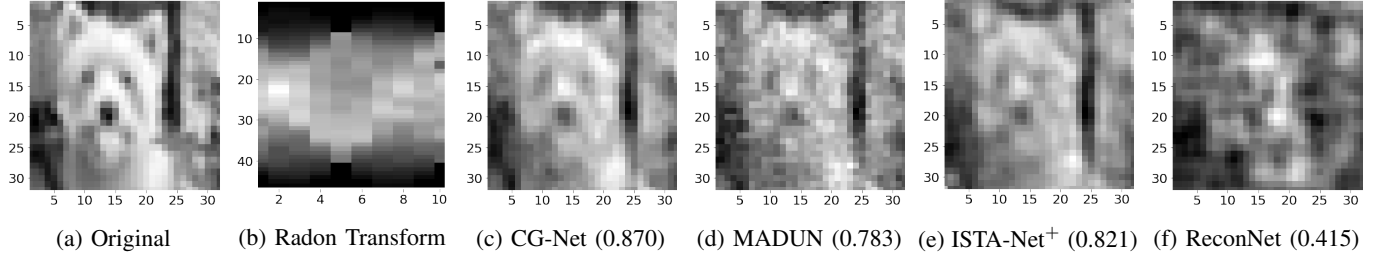


Fig. 6: Test image reconstructions (SSIM) of a 32×32 dog image. Here, Ψ is a Radon transform at 10 uniformly spaced angles, Φ is a biorthogonal wavelet transformation, and the noise level is 60dB SNR. Our method CG-Net (6c) performs best.

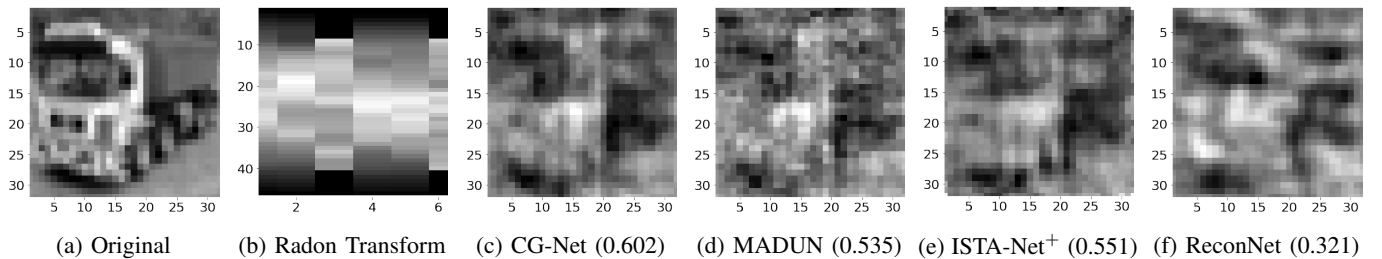


Fig. 7: Test image reconstructions (SSIM) for a 32×32 truck image. Here, Ψ is a Radon transform at 6 uniformly spaced angles, Φ is a biorthogonal wavelet transformation, and the noise level is 60dB SNR. Our method CG-Net (7c) performs best.

experiments, we learn the full lower triangular matrix for each L_k^j . Table III provides the average SSIM and PSNR, across 200 test image reconstructions after training on 2000 measurement, coefficient pairs, with 99% confidence intervals for various Ψ and Φ . Again, CG-Net outperforms or performs comparably to MADUN, ISTA-Net⁺, and ReconNet in these alternative sensing matrices and dictionary schemes.

IV. ABLATION STUDY & TIME REQUIREMENTS

We consider the effect of removing the learned steepest descent matrix B_k^j from CG-Net by fixing it during training. Two possibilities are employed, a gradient CG-Net (gCG-

Net) where $B_k^j = I$ and a Newton CG-Net (nCG-Net) where $B_k^j = \left(H_{F; \mathbf{z}}(\mathbf{u}_{k-1}, \mathbf{z}_k^{j-1}) \right)^{-1}$ where $H_{F; \mathbf{z}}$ is given in (14). Shown in Table IV is the average SSIM of 200 test image reconstructions from Radon transforms at 15, 10, and 6 uniformly spaced angles with a 60dB or 40dB SNR noise level when varying the amount of training data. With fewer than 500 training data samples both gCG-Net and nCG-Net structures perform comparably or outperform the fully general version of CG-Net. Likely, this is due to gCG-Net and nCG-Net having fewer parameters to be fit for these cases and thus avoiding overfitting. With more than 500 training data samples CG-Net begins to perform comparably or outperform gCG-Net and

TABLE III: Average SSIM/PSNR with 99% confidence intervals for four deep learning image reconstruction methods when training and testing on alternative sensing matrices, Ψ , or dictionaries, Φ . Here, $\Psi \in \mathbb{R}^{m \times n}$ is either a Radon transform, at 15 or 10 uniformly spaced angles, as in tomographic imaging or a Gaussian matrix, with 0.5 or 0.3 sampling ratio (defined as $\frac{m}{n}$), as in compressive sensing. Similarly, Φ is either a biorthogonal wavelet or discrete cosine transformation. The measurement noise level is 60dB SNR. Each method reconstructed two hundred 32×32 images after training on a set of 2000 samples. In all cases, our method CG-Net, highlighted in **bold**, performs better or comparably to all other approaches.

Φ	SSIM($\times 10^2$)/PSNR for 32×32 images							
	Discrete Cosine Transformation				Biorthogonal Wavelet Dictionary			
	15 Angles		10 Angles		0.5 sampling ratio		0.3 sampling ratio	
Ψ								
CG-Net	92.1 \pm .49/29.2 \pm .41	83.0 \pm .81/25.4 \pm .41	81.9 \pm .69/24.4 \pm .41	71.0 \pm .92/21.8 \pm .41	88.2 \pm .70/26.3 \pm .35	78.5 \pm .97/23.8 \pm .35	84.6 \pm .70/25.4 \pm .35	78.0 \pm .90/23.2 \pm .39
MADUN	90.6 \pm 1.8/26.5 \pm .41	82.9 \pm .82/25.3 \pm .43	84.2 \pm .70/25.2 \pm .40	68.7 \pm 1.0/21.6 \pm .38	84.6 \pm .70/25.4 \pm .35	78.0 \pm .90/23.2 \pm .39	84.4 \pm .70/24.9 \pm .39	64.0 \pm 1.1/20.3 \pm .36
ISTA-Net ⁺	86.5 \pm .66/24.9 \pm .39	81.5 \pm .83/24.4 \pm .40	84.4 \pm .70/24.9 \pm .39	64.0 \pm 1.1/20.3 \pm .36	84.4 \pm .70/24.9 \pm .39	64.0 \pm 1.1/20.3 \pm .36	84.4 \pm .70/24.9 \pm .39	64.0 \pm 1.1/20.3 \pm .36
ReconNet	68.0 \pm 1.3/22.0 \pm .35	64.2 \pm 1.5/21.5 \pm .38	77.4 \pm 1.0/23.4 \pm .40	65.3 \pm 1.3/21.2 \pm .39	77.4 \pm 1.0/23.4 \pm .40	65.3 \pm 1.3/21.2 \pm .39	77.4 \pm 1.0/23.4 \pm .40	65.3 \pm 1.3/21.2 \pm .39

TABLE IV: Ablation study for CG-Net. Average SSIM ($\times 10^2$) and PSNR for 32×32 image reconstructions from Radon transforms, at a number of uniformly spaced angles, and at a set SNR noise level. We find that gCG-Net and nCG-Net outperform the full version of CG-Net in the low training scenario since fewer parameters must be fit for these cases.

Method	(Angles,SNR)	Training Dataset Size					
		20		100		500	
		SSIM	PSNR	SSIM	PSNR	SSIM	PSNR
gCG-Net	(15,60)	90.0	27.7	90.1	27.8	90.7	28.1
nCG-Net		90.5	28.0	90.6	28.1	90.7	28.1
CG-Net		89.9	27.7	90.3	27.9	91.3	28.4
gCG-Net	(10,60)	81.6	24.8	81.7	24.9	82.3	25.1
nCG-Net		81.8	24.9	81.8	24.9	81.9	24.9
CG-Net		81.5	24.8	81.8	24.9	82.9	25.3
gCG-Net	(6,60)	67.5	21.8	67.8	21.8	68.3	22.0
nCG-Net		67.1	21.7	67.2	21.7	67.3	21.8
CG-Net		67.6	21.8	67.9	21.9	69.0	22.1
gCG-Net	(6,40)	64.1	21.2	64.2	21.3	64.3	21.3
nCG-Net		64.9	21.3	65.0	21.4	64.9	21.4
CG-Net		64.2	21.3	64.7	21.4	66.5	21.6

nCG-Net.

Table V lists the average computational time per image, in seconds, across 200 test image reconstructions running on a 64-bit Intel(R) Xeon(R) CPU E5-2690. We see that CG-LS is slower than the comparative iterative methods although it has yet to be optimized for computational efficiency and speed. Fortunately, the required computational time is reduced by more than a factor of 100 for CG-Net while producing the same or slightly improved quality image reconstructions. Still, CG-Net lags in computational time against the comparative DNN methods that take a fraction of the time to reconstruct an image. This is likely an outcome of the required linear solver to calculate the inverse in (8) to update \mathbf{u} and the required eigendecomposition in (17). Comparatively, MADUN, ISTA-Net⁺, and ReconNet solely consist of convolutions or matrix, vector products that are appreciably faster to implement than linear solvers.

TABLE V: Average reconstruction time of 32×32 images from Radon transform measurements at 15 uniform angles.

Method	nCG-LS	gCG-LS	ℓ_1 -LS	FBP	BCS	CoSaMP
Time (s)	153.6	87.3	0.18	1.5×10^{-3}	0.62	0.40
Method	CG-Net	MADUN	ISTA-Net ⁺	ReconNet		
Time(s)	0.65	2.6×10^{-2}	7.9×10^{-3}	6.5×10^{-4}		

V. CONCLUSION AND FUTURE WORK

Informed by the powerful statistical representation of image coefficients through the compound Gaussian prior, we developed a novel iterative image reconstruction algorithm, named CG-LS, that enforces the CG prior. CG-LS is based upon a regularized least squares estimate of the image coefficients where the regularization, equivalent to the negative log prior from a MAP estimate, is chosen to capture the fundamental statistics of the CG prior. We conducted a rigorous theoretical characterization of CG-LS, which gave important insights into the implementation of the algorithm. Numerical validation of CG-LS was conducted, which showed a significant improvement over state-of-the-art image reconstruction algorithms.

Furthermore, we have applied algorithm unrolling to CG-LS, creating a deep neural network named CG-Net. To the best of our knowledge, CG-Net is the first unrolled DNN for natural and tomographic image reconstruction to be fundamentally informed by a CG prior. Multiple datasets were used to train CG-Net and test CG-Net where, after each training, CG-Net was shown to outperform other unrolled DNNs as well as standard DNNs. In particular, CG-Net significantly outperforms the comparative methods in the low training and sparse sensing regimes for both tomographic imaging and CS applications. Finally, a comparison of the computational time to reconstruct a single image from each iterative and DNN method was discussed. CG-Net significantly improved upon the necessary time over CG-LS, but still falls short of the speed other DNN methods achieve for image reconstruction.

Improving the computational speed of CG-Net serves as one direction of future work for which we suggest two techniques. First, applying the Woodbury matrix identity to (8) gives

$$\mathbf{u}_k = \lambda^{-1} A_{\mathbf{z}_k}^T \mathbf{y} - (A_{\mathbf{z}_k} A_{\mathbf{z}_k}^T + \lambda I)^{-1} A_{\mathbf{z}_k} A_{\mathbf{z}_k}^T \mathbf{y}. \quad (18)$$

Equation (18) transforms an $n \times n$ linear solve in (8) into an $m \times m$ linear solve and as $m \ll n$, we expect a sufficient reduction in computational time. Second, during the training of CG-Net the eigendecomposition in (17) must be implemented within each Z_k^j layer call as the entries of L_k^j are actively being updated and thus, we need to actively ensure $(L_k^j + (L_k^j)^T)/2$ stays positive definite. For the use of CG-Net post-training, the eigendecomposition only needs to be implemented once upon instantiating the model with pre-trained network parameters.

Additionally, an open question remains as to the manner that the CG-Net model can be generalized to replace aspects

of CG-based optimization with relevant neural network structures. For instance, the CG prior depends on the choice of nonlinearity h , or the corresponding choice of its inverse f . A future implementation of CG-Net could learn f by approximating it with a sub-network embedded inside of CG-Net. Such an extension of CG-Net could expand its applicability by both no longer requiring a user-specified function f , as well as providing CG-Net with a greater learning capacity.

VI. APPENDIX

A. Proposition 2 Details

First, a lemma on the eigenvalues of a 2×2 block matrix.

Lemma 6. For $\mathbf{a}, \mathbf{b}, \mathbf{c} \in \mathbb{R}^n$ let $A = D\{\mathbf{a}\}$, $B = D\{\mathbf{b}\}$, and $C = D\{\mathbf{c}\}$. The eigenvalues of $M = \begin{bmatrix} A & B \\ B & C \end{bmatrix}$ are

$$\lambda_i^\pm = (a_i + c_i \pm \sqrt{(a_i - c_i)^2 + 4b_i^2})/2, \quad i = 1, \dots, n.$$

Proof. Note B and $C - rI$ commute. Thus, using [50]

$$\det(M - rI) = \det((A - rI)(C - rI) - B^2),$$

which is zero for $r = \lambda_i^\pm$. \square

We now prove Proposition 2.

Proof of Proposition 2. Let $\rho : \mathbb{R}^n \times \mathcal{Z}^n \rightarrow \mathbb{R}^n$ be given by

$$\rho(\mathbf{u}, \mathbf{z}) = A^T(AD\{\mathbf{z}\}\mathbf{u} - \mathbf{y}). \quad (19)$$

Let $i \in \{1, 2, \dots, n\}$. Define $\mathcal{Z}_i(z) := \{z \in [z_0, b]^n : z_i = z\}$ for $z \in [z_0, b]$. Since $f^2(z)$ is differentiable and achieves a local minimum at $z_0 > 0$, then $f'(z_0)f(z_0) = 0$. Then

$$\mathcal{F}_i(\mathbf{z}) = -2\lambda z_0 v_i(\mathbf{z})^2 \leq 0 \quad \text{for all } \mathbf{z} \in \mathcal{Z}_i(z_0)$$

as $\lambda > 0$ and $\mathbf{v}(\mathbf{z}) = [v_1(\mathbf{z}), \dots, v_n(\mathbf{z})]^T$ and $\mathcal{F}(\mathbf{z}) = [\mathcal{F}_1(\mathbf{z}), \dots, \mathcal{F}_n(\mathbf{z})]^T$ are given in (9) and (10), respectively. Writing $\mathbf{y} = s\tilde{\mathbf{y}}$ we define $\tilde{\mathbf{v}}(\mathbf{z}) = A^T(A_z A_z^T + \lambda I)^{-1}\tilde{\mathbf{y}}$ and

$$\tilde{v}_{\max}(b) = \max_{1 \leq i \leq n} \max_{\mathbf{z} \in \mathcal{Z}_i(b)} |\tilde{v}_i(\mathbf{z})|.$$

Let $\mathbf{z}_b \in \mathcal{Z}_i(b)$. Note, $s^2(\tilde{v}_{\max}(b))^2 \geq s^2\tilde{v}_i(\mathbf{z}_b)^2 = v_i(\mathbf{z}_b)^2$. Hence, if

$$\frac{1}{(\tilde{v}_{\max}(b))^2} \frac{f'(b)f(b)}{b} \geq \frac{\lambda}{\mu} s^2 \quad (20)$$

then $\mu f'(b)f(b) \geq \lambda b s^2 (\tilde{v}_{\max}(b))^2 \geq \lambda b v_i(\mathbf{z}_b)^2$. Thus,

$$\mathcal{F}_i(\mathbf{z}) = -\lambda b v_i(\mathbf{z})^2 + \mu f'(b)f(b) \geq 0 \quad \text{for all } \mathbf{z} \in \mathcal{Z}_i(b).$$

By the Poincare-Miranda theorem [51], when s, λ , and μ satisfy (20) there exists a $\mathbf{z}^* \in [z_0, b]^n$ such that $\mathcal{F}(\mathbf{z}^*) = \mathbf{0}$. Thus, by Lemma 1, $[\mathbf{u}^*, \mathbf{z}^*]$ with $\mathbf{u}^* = \mathbf{z}^* \odot \mathbf{v}(\mathbf{z}^*)$ is a stationary point of (3).

Next, we assume that (20) is satisfied and show the Hessian, $H_F = H_F(\mathbf{u}, \mathbf{z})$, of (3) at $[\mathbf{u}^*, \mathbf{z}^*]$ is positive definite. Note

$$\frac{H_F}{2} = \begin{bmatrix} A_z^T \\ A_u^T \end{bmatrix} \begin{bmatrix} A_z & A_u \end{bmatrix} + \begin{bmatrix} \lambda I & D\{\rho(\mathbf{u}, \mathbf{z})\} \\ D\{\rho(\mathbf{u}, \mathbf{z})\} & \mu D\{\mathbf{h}_f(\mathbf{z})\} \end{bmatrix} \quad (21)$$

for \mathbf{h}_f and ρ given in (15) and (19), respectively. Observe

$$\rho(\mathbf{z} \odot \mathbf{v}(\mathbf{z}), \mathbf{z}) = A^T(A_z A_z^T (A_z A_z^T + \lambda I)^{-1} - I)\mathbf{y} = -\lambda \mathbf{v}(\mathbf{z}).$$

Thus, at $\mathbf{x}^* = [\mathbf{u}^*, \mathbf{z}^*]$, using that $\mathbf{u}^* = \mathbf{z}^* \odot \mathbf{v}(\mathbf{z}^*)$ we have

$$\begin{bmatrix} \lambda I & D\{\rho(\mathbf{x}^*)\} \\ D\{\rho(\mathbf{x}^*)\} & \mu D\{\mathbf{h}_f(\mathbf{z}^*)\} \end{bmatrix} = \begin{bmatrix} \lambda I & -\lambda D\{\mathbf{v}(\mathbf{z}^*)\} \\ -\lambda D\{\mathbf{v}(\mathbf{z}^*)\} & \mu D\{\mathbf{h}_f(\mathbf{z}^*)\} \end{bmatrix}$$

which, by Lemma 6, has eigenvalues

$$\lambda_i^\pm = \lambda(1 + c_i \pm \sqrt{(1 - c_i)^2 + 4v_i(\mathbf{z}^*)^2})/2$$

for $c_i := \frac{\mu}{\lambda} [\mathbf{h}_f(\mathbf{z}^*)]_i = \frac{\mu}{\lambda} (f''(z_i^*)f(z_i^*) + f'(z_i^*)^2)$. Since $f^2(z)$ is strictly convex on $[a, b]$, then $f''(z_i^*)f(z_i^*) + f'(z_i^*)^2 > 0$ implying $c_i > 0$ and thus $\lambda_i^+ > 0$ for all $i = 1, 2, \dots, n$.

Now $\lambda_i^- > 0$ if and only if $c_i > v_i(\mathbf{z}^*)^2$. Define

$$h_{f \min} = \min_{z \in [z_0, b]} f''(z)f(z) + f'(z)^2$$

$$\tilde{v}_{\max} = \max_{1 \leq i \leq n} \max_{\mathbf{z} \in [z_0, b]^n} |\tilde{v}_i(\mathbf{z})|.$$

Note $s^2 \tilde{v}_{\max}^2 \geq s^2 \tilde{v}_i(\mathbf{z}^*)^2 = v_i(\mathbf{z}^*)^2$ and $[\mathbf{h}_f(\mathbf{z}^*)]_i \geq h_{f \min}$ for all $i = 1, 2, \dots, n$. Hence, if

$$\frac{h_{f \min}}{\tilde{v}_{\max}^2} > \frac{\lambda}{\mu} s^2 \quad (22)$$

then $c_i = \frac{\mu}{\lambda} [\mathbf{h}_f(\mathbf{z}^*)]_i \geq \frac{\mu}{\lambda} h_{f \min} > s^2 \tilde{v}_{\max}^2 \geq v_i(\mathbf{z}^*)^2$ and thus $\lambda_i^- > 0$. Therefore, when s, λ , and μ satisfy (22) then (21) at $[\mathbf{u}^*, \mathbf{z}^*]$ is the sum of a positive semi-definite and positive definite matrix, implying the Hessian is positive definite. Lastly, note $f'(b)f(b) > 0$ and $h_{f \min} > 0$ as $f^2(z)$ is strictly convex on $[a, b]$ and achieves a minimizer $z_0 \in (a, b)$. Thus (20) and (22) can be satisfied for positive λ, μ , and s . \square

Comparing (20) and (22) we note $\tilde{v}_{\max}^2 \geq (\tilde{v}_{\max}(b))^2$. Hence, if an approximation of \tilde{v}_{\max} , which we denote by \hat{v}_{\max} , is obtained then we can satisfy both (20) and (22) choosing $\min\{f'(b)f(b)/b, h_{f \min}\}/\hat{v}_{\max}^2 > \lambda s^2/\mu$. Note, for a given f , both $f'(b)f(b)/b$ and $h_{f \min}$ can easily be obtained.

B. Proposition 3 Details

For initial estimates \mathbf{u}_0 and \mathbf{z}_0 , define the sublevel set

$$S(\mathbf{u}_0, \mathbf{z}_0) = \{(\mathbf{u}, \mathbf{z}) \in \mathbb{R}^n \times \mathcal{Z}^n : F(\mathbf{u}, \mathbf{z}) \leq F(\mathbf{u}_0, \mathbf{z}_0)\}.$$

Since F is continuous then $S(\mathbf{u}_0, \mathbf{z}_0)$ is closed and since F is coercive in both \mathbf{u} and \mathbf{z} then $S(\mathbf{u}_0, \mathbf{z}_0)$ is bounded. Thus, $S(\mathbf{u}_0, \mathbf{z}_0)$ is compact, which implies that F has Lipschitz continuous gradient on $S(\mathbf{u}_0, \mathbf{z}_0)$. Let $L := L_z(\mathbf{u}_0, \mathbf{z}_0)$ be the Lipschitz constant, on $S(\mathbf{u}_0, \mathbf{z}_0)$, for $\nabla_z F$.

Proof of Proposition 3. Let $\zeta = \mathbf{z}_k^j$, $\xi = \mathbf{z}_k^{j-1}$, and $\eta = \eta_k^{(j)}$. As ∇G_k is Lipschitz continuous with constant L , then

$$G_k(\zeta) \leq G_k(\xi) + \eta \nabla G_k(\xi)^T \mathbf{d}_k^j(\xi) + \frac{L}{2} \|\eta \mathbf{d}_k^j(\xi)\|_2^2. \quad (23)$$

for sufficiently small η . Using (7) note, $\nabla G_k(\mathbf{x})^T \mathbf{d}_k^j(\mathbf{x}) = -\|\nabla G_k(\mathbf{x})\|_{*(k,j)}^2$ and for the Euclidean bound constant $\gamma_{(k,j)}$ of $\|\cdot\|_{(k,j)}$ we have $\gamma_{(k,j)}^2 \|\mathbf{d}_k^j(\mathbf{x})\|_2^2 \leq \|\nabla G_k(\mathbf{x})\|_{*(k,j)}^2$. Combining with (23) gives

$$G_k(\zeta) \leq G_k(\xi) - \eta \left(1 - \frac{\eta L}{2\gamma_{(k,j)}^2}\right) \|\nabla G_k(\xi)\|_{*(k,j)}^2. \quad (24)$$

From [44] a backtracking line employs two user-chosen parameters $\alpha \in (0, 1/2]$ and $\beta \in (0, 1)$ where the step size η is chosen to be a multiple of β satisfying

$$G_k(\zeta) \leq G_k(\xi) - \alpha\eta \|\nabla G_k(\xi)\|_{*(k,j)}^2. \quad (25)$$

Note, (24) implies (25) when $\eta \leq \gamma_{(k,j)}^2/L$ and thus, from [44], the backtracking line search step size satisfies $\eta \geq \min\{1, \beta\gamma_{(k,j)}^2/L\} > 0$. Combining with (24) and (25) produces (11) when $c_{(k,j)} = \alpha \min\{1, \beta\gamma_{(k,j)}^2/L\}$. \square

C. Theorem 4 Details

Recall $G_k(\mathbf{z}) = F(\mathbf{u}_{k-1}, \mathbf{z})$. We now prove Theorem 4.

Proof of Theorem 4. Define $\mathbf{v}_k = [\mathbf{u}_k, \mathbf{z}_k]$, $\mathbf{v}_{k-\frac{1}{2}} = [\mathbf{u}_{k-1}, \mathbf{z}_k]$ and $\mathbf{v}_{k-\frac{1}{2}}^j = [\mathbf{u}_{k-1}, \mathbf{z}_k^j]$. We let $F(\mathbf{v}_k) = F(\mathbf{u}_k, \mathbf{z}_k)$ and similarly for $F(\mathbf{v}_{k-\frac{1}{2}}^j)$ and $F(\mathbf{v}_{k-\frac{1}{2}})$. Note, for all $k \geq 1$, $\mathbf{v}_{k-\frac{1}{2}}^0 = \mathbf{v}_{k-1}$ and $\mathbf{v}_{k-\frac{1}{2}}^J = \mathbf{v}_{k-\frac{1}{2}}$. Summing over j in (11)

$$\begin{aligned} F(\mathbf{v}_{k-1}) - F(\mathbf{v}_{k-\frac{1}{2}}) &\geq \sum_{j=1}^J c_{(k,j)} \left\| \nabla_{\mathbf{z}} F(\mathbf{v}_{k-\frac{1}{2}}^j) \right\|_{*(k,j)}^2 \\ &\geq c_{(k,1)} \left\| \nabla_{\mathbf{z}} F(\mathbf{v}_{k-1}) \right\|_{*(k,1)}^2. \end{aligned} \quad (26)$$

First, note $\nabla_{\mathbf{u}} F(\mathbf{v}_{k-1}) = \mathbf{0}$ since \mathbf{u}_{k-1} is a global minimizer of (3) with \mathbf{z} fixed at \mathbf{z}_{k-1} . Hence, we have $\left\| \nabla_{\mathbf{z}} F(\mathbf{v}_{k-1}) \right\|_{*(k,1)}^2 = \left\| \nabla F(\mathbf{v}_{k-1}) \right\|_{*(k,1)}^2$. Second, note $F(\mathbf{v}_k) \leq F(\mathbf{v}_{k-\frac{1}{2}})$ since \mathbf{u}_k is a global minimizer of (3) with \mathbf{z} fixed at \mathbf{z}_k . Hence, $-F(\mathbf{v}_k) \geq -F(\mathbf{v}_{k-\frac{1}{2}})$. Third, define

$$c := \alpha \min\{1, \beta\gamma^2/L\} \quad (27)$$

and note, since $\gamma_{(k,1)} \geq \gamma$, then, from Proposition 3 $c_{(k,1)} \geq c > 0$. Combining these three results with (26) gives

$$F(\mathbf{v}_{k-1}) - F(\mathbf{v}_k) \geq c \left\| \nabla F(\mathbf{v}_{k-1}) \right\|_{*(k,1)}^2. \quad (28)$$

Thus, CG-LS generates a monotonic decreasing sequence of cost function values, which are bounded below by 0. Hence, $\{F(\mathbf{v}_k)\}_{k=0}^{\infty}$ converges to a value F^* . Therefore, taking an infinite sum of (28) w.r.t k and using $\gamma_{*(k,1)} \geq \gamma$ gives

$$F(\mathbf{v}_0) - F^* \geq c \sum_{k=1}^{\infty} \left\| \nabla F(\mathbf{v}_{k-1}) \right\|_{*(k,1)}^2 \geq \gamma^2 c \sum_{k=0}^{\infty} \left\| \nabla F(\mathbf{v}_k) \right\|_2^2.$$

Implying that $\sum_{k=0}^{\infty} \left\| \nabla F(\mathbf{v}_k) \right\|_2^2$ converges. Thus, $\lim_{k \rightarrow \infty} \left\| \nabla F(\mathbf{v}_k) \right\|_2^2 \rightarrow 0$ and so $\lim_{k \rightarrow \infty} \nabla F(\mathbf{v}_k) \rightarrow \mathbf{0}$. Finally, taking an average of (28) gives

$$\frac{F(\mathbf{v}_0) - F(\mathbf{v}_K)}{c} \frac{1}{K} \geq \min_{1 \leq k \leq K} \left\| \nabla F(\mathbf{v}_k) \right\|_{*(k,1)}^2. \quad \square$$

D. Theorem 5 Details

First, define

$$\mathcal{B}_\delta(\hat{\mathbf{u}}, \hat{\mathbf{z}}) = \{[\mathbf{u}, \mathbf{z}] \in \mathbb{R}^n \times \mathcal{Z}^n : \left\| [\mathbf{u}, \mathbf{z}] - [\hat{\mathbf{u}}, \hat{\mathbf{z}}] \right\|_2 < \delta\}.$$

for $\delta > 0$, $\hat{\mathbf{u}} \in \mathbb{R}^n$, and $\hat{\mathbf{z}} \in \mathcal{Z}^n$. We now prove Theorem 5.

Proof of Theorem 5. The non-degenerate local minimizer $[\mathbf{u}^*, \mathbf{z}^*]$ in Proposition 2 satisfies, for all $\mathbf{w} \in \mathbb{R}^{2n}$, $\mathbf{w}^T H_F(\mathbf{u}^*, \mathbf{z}^*) \mathbf{w} = \ell_0(\mathbf{w}) \geq \lambda_{\min} > 0$ where λ_{\min} is the

minimum eigenvalue of the Hessian $H_F(\mathbf{u}^*, \mathbf{z}^*)$. Since (3) is twice continuously differentiable then, for fixed $\mathbf{w} \in \mathbb{R}^{2n}$, $Q(\mathbf{u}, \mathbf{z}) := \mathbf{w}^T H_F(\mathbf{u}, \mathbf{z}) \mathbf{w}$ is a continuous function. Fix $\ell \in (0, \lambda_{\min})$ and let $\epsilon = \lambda_{\min} - \ell > 0$. By continuity of Q there exists a $\delta > 0$ such that for all $[\mathbf{u}, \mathbf{z}] \in \mathcal{B}_\delta(\mathbf{u}^*, \mathbf{z}^*)$ we have $|Q(\mathbf{u}, \mathbf{z}) - Q(\mathbf{u}^*, \mathbf{z}^*)| < \epsilon = \lambda_{\min} - \ell$, which implies $Q(\mathbf{u}, \mathbf{z}) \geq \ell$. Therefore, (3) is strongly convex with constant ℓ on $\mathcal{C} = \mathcal{B}_\delta(\mathbf{u}^*, \mathbf{z}^*)$.

Next, strong convexity of (3) with constant ℓ implies that

$$F(\mathbf{v}_i) - F^* \leq (2\ell)^{-1} \left\| \nabla F(\mathbf{v}_i) \right\|_2^2 \quad (29)$$

for all $i \geq 0$. Rearranging (28), subtracting F^* from both sides, and applying $\|\cdot\|_{*(k,1)} \geq \gamma \|\cdot\|_2$ gives

$$F(\mathbf{v}_k) - F^* \leq F(\mathbf{v}_{k-1}) - F^* - \gamma^2 c \left\| \nabla F(\mathbf{v}_{k-1}) \right\|_2^2,$$

which combined with (29), when $i = k-1$, produces

$$F(\mathbf{v}_k) - F^* \leq (1 - 2\ell\gamma^2 c) (F(\mathbf{v}_{k-1}) - F^*). \quad (30)$$

Applying (30) recursively gives (12). \square

E. Compound Gaussian Representations

Here, we discuss the generality of the CG prior.

Proposition 7. *The generalized Gaussian, student's t , α -stable, and symmetrized Gamma distributions are special cases of the compound Gaussian distribution.*

The result of Proposition 7 is found in [9, 10]. Now, we give an explicit nonlinearity, h , such that the CG prior reduces to a Laplace prior.

Proposition 8. *Let Υ be the cumulative distribution function (CDF) of a standard Gaussian random variable. Define*

$$h(x) = (-2\lambda^2 \ln(1 - \Upsilon(x)))^{1/2}.$$

Then $\mathbf{c} = h(\mathbf{x}) \odot \mathbf{u}$, for $\mathbf{x} \sim \mathcal{N}(\mathbf{0}, I)$ and $\mathbf{u} \sim \mathcal{N}(\mathbf{0}, I)$, has a Laplace distribution. That is, $\mathbf{c} \sim \lambda \exp(-\lambda \|\mathbf{c}\|_1)/2$.

Proof. A Laplace random variable $X \sim \lambda \exp(-\lambda x)/2$ is decomposed as $X = \sqrt{Z}U$, for $U \sim \mathcal{N}(0, 1)$ and $Z \sim \text{Exp}(1/2\lambda^2)$. Let $F_Z(z) = 1 - e^{-z/(2\lambda^2)}$ be the CDF of Z . Due to independence in the components of \mathbf{c} , we only need to show that $h(x_i)^2 \sim Z$ for $x_i \sim \mathcal{N}(0, 1)$, which is easily observed since

$$\mathbb{P}(h(x_i)^2 \leq x) = \mathbb{P}(x_i \leq \Upsilon^{-1}(F_Z(x))) = F_Z(x). \quad \square$$

REFERENCES

- [1] S. Foucart and H. Rauhut, *A Mathematical Introduction to Compressive Sensing*. Springer, 2013.
- [2] A. Beck and M. Teboulle, "A Fast Iterative Shrinkage-Thresholding Algorithm for Linear Inverse Problems," *SIAM Journal on Imaging Sciences*, vol. 2, no. 1, pp. 183–202, 2009.
- [3] S. Ji, Y. Xue, and L. Carin, "Bayesian Compressive Sensing," *IEEE Transactions on Signal Processing*, vol. 56, no. 6, pp. 2346–2356, 2008.
- [4] D. Needell and J. A. Tropp, "CoSaMP: Iterative signal recovery from incomplete and inaccurate samples," *Applied and Computational Harmonic Analysis*, vol. 26, pp. 301–321, 2009.
- [5] I. Daubechies, M. DeFrise, and C. De Mol, "An Iterative Thresholding Algorithm for Linear Inverse Problems with a Sparsity Constraint," *Communications on Pure and Applied Mathematics*, vol. 57, no. 11, pp. 1413–1457, 2004.

- [6] S.-J. Kim, K. Koh, M. Lustig, S. Boyd, and D. Gorinevsky, "An Interior-Point Method for Large-Scale ℓ_1 -Regularized Least Squares," *IEEE Journal of Selected Topics in Signal Processing*, vol. 1, no. 4, pp. 606–617, 2007.
- [7] R. G. Raj, "A hierarchical Bayesian-MAP approach to inverse problems in imaging," *Inverse Problems*, vol. 32, no. 7, p. 075003, 2016.
- [8] J. McKay, R. G. Raj, and V. Monga, "Fast stochastic hierarchical Bayesian map for tomographic imaging," in *2017 51st Asilomar Conference on Signals, Systems, and Computers*. IEEE, 2017, pp. 223–227.
- [9] M. J. Wainwright and E. P. Simoncelli, "Scale Mixtures of Gaussians and the Statistics of Natural Images," in *Advances in Neural Information Processing Systems*, vol. 12. MIT Press, 1999, pp. 855–861.
- [10] M. J. Wainwright, E. P. Simoncelli, and A. S. Willsky, "Random Cascades on Wavelet Trees and Their Use in Analyzing and Modeling Natural Images," *Applied and Computational Harmonic Analysis*, vol. 11, no. 1, pp. 89–123, 2001.
- [11] Z. Chance, R. G. Raj, and D. J. Love, "Information-theoretic structure of multistatic radar imaging," in *2011 IEEE RadarCon (RADAR)*. IEEE, 2011, pp. 853–858.
- [12] K. Kulkarni, S. Lohit, P. Turaga, R. Kerviche, and A. Ashok, "ReconNet: Non-Iterative Reconstruction of Images From Compressively Sensed Measurements," in *Proceedings of the IEEE Conference on Computer Vision and Pattern Recognition*, 2016, pp. 449–458.
- [13] A. Bora, A. Jalal, E. Price, and A. G. Dimakis, "Compressed Sensing using Generative Models," in *Proceedings of the International Conference on Machine Learning*, vol. 70. PMLR, 2017, pp. 537–546.
- [14] C. Qin, J. Schlemper, J. Caballero, A. N. Price, J. V. Hajnal, and D. Rueckert, "Convolutional Recurrent Neural Networks for Dynamic MR Image Reconstruction," *IEEE Transactions on Medical Imaging*, vol. 38, no. 1, pp. 280–290, 2019.
- [15] D. Liang, J. Cheng, Z. Ke, and L. Ying, "Deep Magnetic Resonance Image Reconstruction: Inverse Problems Meet Neural Networks," *IEEE Signal Processing Magazine*, vol. 37, no. 1, pp. 141–151, 2020.
- [16] A. Lucas, M. Iliadis, R. Molina, and A. K. Katsaggelos, "Using Deep Neural Networks for Inverse Problems in Imaging: Beyond Analytical Methods," *IEEE Signal Processing Magazine*, vol. 35, no. 1, pp. 20–36, 2018.
- [17] G. Wang, J. C. Ye, and B. De Man, "Deep learning for tomographic image reconstruction," *Nature Machine Intelligence*, vol. 2, no. 12, pp. 737–748, 2020.
- [18] S. S. Chandra, M. Bran Lorenzana, X. Liu, S. Liu, S. Bollmann, and S. Crozier, "Deep learning in magnetic resonance image reconstruction," *Journal of Medical Imaging and Radiation Oncology*, vol. 65, no. 5, pp. 564–577, 2021.
- [19] K. Gregor and Y. LeCun, "Learning fast approximations of sparse coding," in *Proceedings of the 27th International Conference on Machine Learning*, 2010, pp. 399–406.
- [20] V. Monga, Y. Li, and Y. C. Eldar, "Algorithm Unrolling: Interpretable, efficient deep learning for signal and image processing," *IEEE Signal Processing Magazine*, vol. 38, no. 2, pp. 18–44, 2021.
- [21] J. Song, B. Chen, and J. Zhang, "Memory-Augmented Deep Unrolling Network for Compressive Sensing," in *Proceedings of the 29th ACM International Conference on Multimedia*, 2021, pp. 4249–4258.
- [22] J. Zhang and B. Ghanem, "ISTA-Net: Interpretable Optimization-Inspired Deep Network for Image Compressive Sensing," in *Proceedings of the IEEE Conference on Computer Vision and Pattern Recognition*, 2018, pp. 1828–1837.
- [23] K. H. Jin, M. T. McCann, E. Froustey, and M. Unser, "Deep Convolutional Neural Network for Inverse Problems in Imaging," *IEEE Transactions on Image Processing*, vol. 26, no. 9, pp. 4509–4522, 2017.
- [24] Y. Yang, J. Sun, H. Li, and Z. Xu, "ADMM-CSNet: A Deep Learning Approach for Image Compressive Sensing," *IEEE Transactions on Pattern Analysis and Machine Intelligence*, vol. 42, no. 3, pp. 521–538, 2020.
- [25] T. Meinhardt, M. Moller, C. Hazirbas, and D. Cremers, "Learning Proximal Operators: Using Denoising Networks for Regularizing Inverse Imaging Problems," in *Proceedings of the IEEE International Conference on Computer Vision*, 2017, pp. 1781–1790.
- [26] S. Diamond, V. Sitzmann, F. Heide, and G. Wetzstein, "Unrolled Optimization with Deep Priors," *arXiv preprint arXiv:1705.08041*, 2019.
- [27] U. Schmidt and S. Roth, "Shrinkage Fields for Effective Image Restoration," in *2014 IEEE Conference on Computer Vision and Pattern Recognition*, 2014, pp. 2774–2781.
- [28] C. Lyons, R. G. Raj, and M. Cheney, "CG-Net: A Compound Gaussian Prior Based Unrolled Imaging Network," in *2022 IEEE Asia-Pacific Signal and Information Processing Association Annual Summit and Conference*, 2022, pp. 623–629.
- [29] M. Bertero, C. De Mol, and E. R. Pike, "Linear inverse problems with discrete data: II. Stability and regularisation," *Inverse Problems*, vol. 4, no. 3, p. 573, 1988.
- [30] L. Ying, D. Xu, and Z.-P. Liang, "On Tikhonov regularization for image reconstruction in parallel MRI," in *Proceedings of the 26th Annual International Conference of the IEEE Engineering in Medicine and Biology Society*, vol. 1. IEEE, 2004, pp. 1056–1059.
- [31] J. M. Bioucas-Dias and M. A. T. Figueiredo, "A New TwIST: Two-Step Iterative Shrinkage/Thresholding Algorithms for Image Restoration," *IEEE Transactions on Image Processing*, vol. 16, no. 12, pp. 2992–3004, 2007.
- [32] J. Dahl, P. C. Hansen, S. H. Jensen, and T. L. Jensen, "Algorithms and software for total variation image reconstruction via first-order methods," *Numerical Algorithms*, vol. 53, no. 1, pp. 67–92, 2010.
- [33] Y. Xiao, J. Yang, and X. Yuan, "Alternating algorithms for total variation image reconstruction from random projections," *Inverse Problems & Imaging*, vol. 6, no. 3, p. 547, 2012.
- [34] J. Liu, Y. Sun, C. Eldeniz, W. Gan, H. An, and U. S. Kamilov, "RARE: Image Reconstruction Using Deep Priors Learned Without Groundtruth," *IEEE Journal of Selected Topics in Signal Processing*, vol. 14, no. 6, pp. 1088–1099, 2020.
- [35] J. Wang, A. Dogandžić, and A. Nehorai, "Maximum Likelihood Estimation of Compound-Gaussian Clutter and Target Parameters," *IEEE Transactions on Signal Processing*, vol. 54, no. 10, pp. 3884–3898, 2006.
- [36] Z. Idriss, R. G. Raj, and R. M. Narayanan, "Waveform Optimization for Multistatic Radar Imaging Using Mutual Information," *IEEE Transactions on Aerospace and Electronics Systems*, vol. 57, no. 4, pp. 2410–2425, 2021.
- [37] J. Portilla, V. Strela, M. J. Wainwright, and E. P. Simoncelli, "Image Denoising Using Scale Mixtures of Gaussians in the Wavelet Domain," *IEEE Transactions on Image Processing*, vol. 12, no. 11, pp. 1338–1351, 2003.
- [38] T. Huang, W. Dong, X. Yuan, J. Wu, and G. Shi, "Deep Gaussian Scale Mixture Prior for Spectral Compressive Imaging," in *Proceedings of the IEEE/CVF Conference on Computer Vision and Pattern Recognition*, 2021, pp. 16216–16225.
- [39] I. Goodfellow, Y. Bengio, and A. Courville, *Deep Learning*. MIT press, 2016.
- [40] H. Zhao, O. Gallo, I. Frosio, and J. Kautz, "Loss Functions for Image Restoration With Neural Networks," *IEEE Transactions on Computational Imaging*, vol. 3, no. 1, pp. 47–57, 2017.
- [41] S. J. Wright, "Coordinate descent algorithms," *Mathematical Programming*, vol. 151, no. 1, pp. 3–34, 2015.
- [42] L. Grippo and M. Sciandrone, "On the convergence of the block nonlinear Gauss–Seidel method under convex constraints," *Operations Research Letters*, vol. 26, no. 3, pp. 127–136, 2000.
- [43] A. Beck and L. Tetruashvili, "On the Convergence of Block Coordinate Descent Type Methods," *SIAM Journal on Optimization*, vol. 23, no. 4, pp. 2037–2060, 2013.
- [44] S. Boyd and L. Vandenberghe, *Convex Optimization*. Cambridge University Press, 2004.
- [45] A. Krizhevsky, "Learning Multiple Layers of Features from Tiny Images," University of Toronto, Tech. Rep., 2009.
- [46] L. Fei-Fei, R. Fergus, and P. Perona, "Learning Generative Visual Models from Few Training Examples: An Incremental Bayesian Approach Tested on 101 Object Categories," in *Conference on Computer Vision and Pattern Recognition Workshop*, 2004, pp. 178–178.
- [47] S. R. Deans, *The Radon Transform and Some of Its Applications*. Dover, 2007.
- [48] D. P. Kingma and J. L. Ba, "Adam: A Method for Stochastic Optimization," *International Conference on Learning Representations*, 2015.
- [49] A. G. Baydin, B. A. Pearlmutter, A. A. Radul, and J. M. Siskind, "Automatic Differentiation in Machine Learning: a Survey," *Journal of Machine Learning Research*, vol. 18, 2018.
- [50] J. R. Silvester, "Determinants of Block Matrices," *The Mathematical Gazette*, vol. 84, no. 501, pp. 460–467, 2000.
- [51] W. Kulpa, "The Poincaré–Miranda Theorem," *The American Mathematical Monthly*, vol. 104, no. 6, pp. 545–550, 1997.